Predicting the amplitude and runup of the water waves induced by rotational cliff collapse, considering fragmentation

Hasnain Gardezi[a*], Talha Khan[c], Xingyue Li[a,b*], Taimur Mazhar Sheikh[a], Yu Huang[a,b], Zhiyi Chen[a]

[a] Department of Geotechnical Engineering, College of Civil Engineering, Tongji University, Shanghai 200092, China

[b] State Key Laboratory of Disaster Reduction in Civil Engineering, Tongji University, Shanghai 200092, China

[c] School of Aerospace Engineering and Applied Mechanics, Tongji University, Shanghai 200092, China

*Corresponding authors: ~~hasnain_haider@tongji.edu.cn~~hasnain_haider@tongji.edu.cn (Hasnain Gardezi), ~~xingyueli@tongji.edu.cn~~ xingyueli@tongji.edu.cn (X.Y.Li~~)~~).

Abstract:

Cliff ~~collapse-induced water waves~~ collapses in small lakes and reservoirs ~~retain their energy due to short travel distance, and may cause significant damage to~~ induce powerful waves, threatening the offshore infrastructure. ~~Previously, scientists have analyzed the~~ Unlike previous studies on waves induced by granular~~/block sliding down the slope and hitting a water body, but none have studied the water waves induced by rotational cliff collapse, fragmenting upon impact with the water surface. So,~~ in slide, this study~~, we have~~ experimentally and numerically ~~analyzed~~investigates the waves induced by rotational cliff collapse ~~and energy transfer mechanism, determined~~, whereby the cliff fragments upon impact with the water surface, and determines the wave amplitude ~~and~~, runup ~~of the induced waves, and developed machine learning-based prediction models. Moreover, the effect of the fragmentation of the cliff upon impact on the induced wave has also been investigated. The results~~, and energy transfer mechanics. Results indicate that as the water depth ~~decreases~~decreased, the impact Froude number and relative wave amplitude ~~increase~~increased, wave velocity ~~decreases~~decreased, and ~~the~~ splash ~~becomes more elongated. A comparison between the wave induced by fragmented cliff collapse and~~ showed greater elongation. The numerical modelling results also confirmed the experimental trends. Moreover, compared to an equivalent amount of granular mass sliding ~~from~~down a 30° slope~~ indicates that the amplitude of the waves induced by granular mass is 42%, 35%, and~~, rotational cliff collapse produced 28%~~ less than that of fragmented cliff collapse. The wave amplitude induced by fragmented cliff collapse indicates that the rotational motion of the cliff imparts a more sudden and concentrated impact that allows an efficient energy transfer to water, resulting in~~ 42% higher wave amplitudes~~. The results for~~ due to the acute impact that transfers energy more efficiently. Machine learning based prediction ~~model indicate that~~ models were subsequently developed to predict the wave amplitude and

Formatted: Header

Style Definition: Normal: Font: (Default) +Body (等线), (Asian) +Body Asian (等线), 五号, (Asian) Chinese (Simplified, Mainland China), (Other) English (United Kingdom), Ligatures: Standard + Contextual, Justified, Adjust space between Latin and Asian text, Adjust space between Asian text and numbers

Style Definition: Heading 1

Style Definition: List Paragraph: Font: (Default) +Body (等线), (Asian) +Body Asian (等线), 五号, (Asian) Chinese (Simplified, Mainland China), (Other) English (United Kingdom), Ligatures: Standard + Contextual, Justified, Indent: Left: 0 cm, First line: 2 ch, Space Before: 0 pt, Adjust space between Latin and Asian text, Adjust space between Asian text and numbers

Style Definition: Body Text

Style Definition: Table Paragraph

Formatted

Formatted

Formatted: Normal, Centered, Space Before: 0 pt, Line spacing: 1.5 lines, No bullets or numbering, Tab stops: Not at 15.87 ch

Formatted

Formatted

Formatted

Formatted: Normal, Left, Line spacing: 1.5 lines, No bullets or numbering, Tab stops: Not at 5.87 ch

Formatted

Formatted

Formatted: Normal, Left, Line spacing: 1.5 lines, No bullets or numbering, Tab stops: Not at 5.87 ch

Formatted

Formatted

Formatted

Formatted

Formatted: Normal, Left, Space Before: 0 pt, Line spacing: 1.5 lines, No bullets or numbering, Tab stops: Not at 5.87 ch

Formatted: Font: (Default) Times New Roman, 小四, Bold, Not Expanded by / Condensed by

Formatted: Font: (Default) Times New Roman

Formatted

Formatted

Formatted

Formatted: Font: (Default) Times New Roman, Font color: Red, Not Expanded by / Condensed by

Formatted

Formatted

Formatted

Formatted

Formatted

Formatted

Formatted: Font: (Default) Times New Roman, Font color: Red, Not Expanded by / Condensed by

Formatted

runup model . The prediction models performed well both in the training and testing stages, with higherhigh R^2

Formatted: Header

Formatted: Font: (Default) Times New Roman, Font color: Red

Formatted: Font: (Default) Times New Roman, Font color: Red

Formatted: Font: (Default) Times New Roman, Font color: Red, Not Expanded by / Condensed by

Formatted: Font: (Default) Times New Roman, Font color: Red

Formatted: Font: (Default) Times New Roman, Font color: Red, Not Expanded by / Condensed by

Formatted: Font: (Default) Times New Roman, Font color: Red

Formatted: Font: (Default) Times New Roman, Font color: Red, Not Expanded by / Condensed by

Formatted: Font: (Default) Times New Roman, Font color: Red

Formatted: Font: (Default) Times New Roman, Font color: Red, Not Expanded by / Condensed by

Formatted: Font: (Default) Times New Roman, Font color: Red

Formatted: Font: (Default) Times New Roman, Font color: Red, Not Expanded by / Condensed by

Formatted: Font: (Default) Times New Roman, Font color: Red

Formatted: Font: (Default) Times New Roman, Font color: Red, Not Expanded by / Condensed by

Formatted: Font: (Default) Times New Roman, Font color: Red

Formatted: Font: (Default) Times New Roman, Font color: Red, Not Expanded by / Condensed by

Formatted: Font: (Default) Times New Roman, Font color: Red

Formatted: Font: (Default) Times New Roman, Font color: Red, Not Expanded by / Condensed by

Formatted: Font: (Default) Times New Roman, Font color: Red

Formatted: Font: (Default) Times New Roman, Font color: Red, Not Expanded by / Condensed by

Formatted: Font: (Default) Times New Roman, Font color: Red

Formatted: Font: (Default) Times New Roman, Font color: Red, Not Expanded by / Condensed by

Formatted: Font: (Default) Times New Roman, Font color: Red, Not Expanded by / Condensed by values~~. The developed model was~~, and were validated ~~by comparing the results with~~via established statistical indices ~~and by performing~~, sensitivity, and parametric analysis~~, highlighting that wave amplitude is greatly influenced by~~. The prediction models highlighted a cumulative 90% contribution of impact velocity, cliff height, and the number of fragments~~, contributing approximately 90% to~~ on the wave amplitude. In comparison, runup ~~is~~was greatly influenced by bank slope angle, impact velocity, cliff mass, and height. The experimental results and developed prediction models can provide the basis for understanding the rotational cliff collapse-induced waves and can help with disaster mitigation and risk assessment by effectively predicting the wave amplitude and runup.

Keywords: ~~Rotational~~Cliff fragmentation; landslide tsunami; prediction models; rotational cliff collapse~~,~~; wave amplitude, and runup~~, cliff fragmentation,~~.
~~prediction model.~~

1. ~~1.~~ Introduction

The phenomenon of cliff overturning is common along rivers and reservoirs (glacial lakes, recreational lakes~~), and has been captured by various people around the globe.~~). The cliffs around these lakes are weathered due to climate change and wave action (Ró and Cerkowniak, 2024; Young et al., 2021) and can no longer be supported by the parent rock. When these initially intact, weathered cliffs fall into water, they usually fragment upon impact with the water surface, and as a result, induce an impulse water wave. Upon impact, the energy of gravitational mass is transferred to the water body, resulting in a huge splash and a wave train, propagating away from the point of impact. In the reservoirs and water channels located in mountainous regions, such as glacial lakes, dams, and a river flowing through valleys, these waves do not travel a long distance before reaching obstacles, opposite shores, or other infrastructure. As the waves retain most of their energy, size, and strength, the impact can cause significant damage to the population and infrastructure located along the banks of the reservoir. Historically, extreme impulse wave heights have been observed induced by landslides in events of 1958 Lituya Bay, USA, which caused a wave height of 524 m (Boultbee et al., 2006; Franco et al., 2020; Miller, 1960a)~~1960)~~, 2007 Chehalis Lake, Canada, induced a wave of 38 m (Wang et al., 2015)~~)~~, 2015 Taan Fjord, USA, caused a wave of 193 m (Higman et al., 2018)~~)~~, and 2014 Lake Askaja (Gylfadóttir et al., 2017). More recently, a volcanic activity in 2018 at Anak Krakatoa, Indonesia, triggered a tsunami reaching up to a height of 13 m, and in 2023, the Dickson Fjord ice-rock avalanche caused a wave ~~).~~

Formatted: Header
Formatted: Normal, Left, Indent: First line: 0.74 cm, Line spacing: 1.5 lines, No bullets or numbering, Tab stops: Not at 5.87 ch
Formatted: Font: (Default) Times New Roman, 小四, Bold, Not Expanded by / Condensed by
Formatted: List Paragraph, Left, Line spacing: 1.5 lines, Outline numbered + Level: 1 + Numbering Style: 1, 2, 3, … + Start at: 1 + Alignment: Left + Aligned at: 0 cm + Indent at: 0.63 cm, Tab stops: Not at 5.87 ch
Formatted: Font: (Default) Times New Roman, Font color: Black, Not Expanded by / Condensed by

Moreover, the highly energetic gravity waves are capable of overtopping the dam wall, especially where the freeboard is just a few meters. The overtopping can result in dam failure and can lead to catastrophic events, such as caused by 1963 Vajont rock slide, in North Italy, where a 250 Mm^3 of rock mass slid into the dam reservoir and induced a huge wave that ran to a height of 200 m at the opposite bank (Franci(Svennevig et al., 2024). 2020; Heller and Ruffini, 2023; Ward, N. Steve and Day, Simon, 2011; Zhao et al., 2016), the resultant wave overtopped the dam and destroyed an entire village downstream. Similarly, in 2003 Qianjiangping landslide with a volume of 24 Mm^3, and in 2008 Gongjiafang landslide with a volume of 0.38Mm^3 in Three Gorges dam reservoir area induced a water wave that had an amplitude of 30 m and 32 m respectively (Wang et al., 2021), Gongjiafang landslide induced wave ran up to a height of 12.4 m on opposite bank (Huang et al., 2012).

These incidents highlight the need for predicting the subsequent energy transfer of such cliff collapses for disaster mitigation. The wave amplitude and runup height are of great importance. In contrast, the The cases mentioned above are extreme;, whereas the smallphenomena of sliding, toppling, and falling eventsof cliffs in small lakes and reservoirs can induce a wave of comparably small amplitude but capable of causing substantial damage to densely populated areas along the shoreline. Particularly, in the case of glacial lakes, recreational lakes, and lakes formed by previous landslides are prone to cause major disasters as they are considerably smaller compared to dam reservoirs (Gardezi et al., 2021). The phenomena of cliff overturning and falling are common around these lakes quite frequent and have been captured by various people around the globe. Fig. 1 (a, b, and c) indicates a rotational (topple) cliff collapse in Furnas Lake, Brazil, on 8 January 2022, killing 10 people (Maciel et al., 2023; Sun et al., 2024). As a result of the collapse, a huge splash and induced waves can be seen in Fig. 1 (c). Though scientists have analyzed the amplitude and runup of the waves induced by sliding masses, the literature lacks in providing detailed informationDespite recurring events of cliff collapse along the water banks, the rotational failure of cliffs accompanied by fragmentation upon impact with the water surface remains poorly understood. Recent studies on the formation and propagation of the wave induced by rotational cliff collapse. Moreover, the literature also lacks in elaboratingwater waves have focused on the shape of the induced splash. Effect of cliff fragmentation on the induced wave, as can be seen in Fig. 1 (a, b, and c), the falling cliff was still intact and broke under its own weight upon impact with the water surface

Formatted: Header

Formatted: Font: (Default) Times New Roman, Font color: Red, Ligatures: None

Formatted

Formatted: Normal, Left, Indent: First line: 0.63 cm, Line spacing: 1.5 lines, No bullets or numbering, Tab stops: Not at 5.87 ch

Formatted

Formatted

Formatted

Formatted

Formatted

Formatted: Font: (Default) Times New Roman

Formatted

Formatted

Formatted

Formatted

and induced a huge splash. Furthermore, though there are numerous prediction models available for the amplitude and runup of landslide-induced water waves, the prediction models for water waves induced by rotational fall of cliffs considering fragmentation are nonexistent.

Field data related to historical events is critical for disaster mitigation, but due to their occurrence in remote areas, the unavailability of measuring devices makes it difficult, leaving the physical modeling as the only source for understanding the wave generation, and propagation phenomena (Bellotti and Romano, 2017; Grilli et al., 2017; Takabatake et al., 2022; Wang et al., 2017a; Watts, 1998a). Previously, scientists have performed both two, and three dimensional physical modeling for landslide induced water waves using either block slide (Heinrich, 1992; Heller and Spinneken, 2013; Najafi-Jilani and Ataie-Ashtiani, 2008; Sælevik et al., 2009), (M. Di Risio et al., 2009; Marcello Di Risio et al., 2009; Lindstrøm et al., 2014; Montagna et al., 2011; Panizzo et al., 2005; Wang et al., 2016)block slides, translational slides, or granular slide (Fritz et al., 2003a, 2003b; Lindstrøm, 2016; Miller et al., 2016; Zweifel et al., 2006),(flows, where the mass moves along a predefined basal plane. Moreover, physical modeling has also been carried out to analyse the amplitude and runup of the landslides-induced water waves either by using block slide or granular slide (Heller and Spinneken, 2015; Huang, 2013; Lindstrøm, 2016; Lindstrøm et al., 2014; McFall and Fritz, 2016; Miller, 1960; Mohammed and Fritz, 2012; Montagna et al., 2011; Romano et al., 2023, 2020; Sælevik et al., 2009; Yin et al., 2015). However, the rotational collapse is different from the type of failure mentioned above. In rotational collapse, the cliff rotates along the base and falls into water, thus inducing a huge splash and fragmenting upon impact. Romano et al., 2023),

But none have developed a physical model to quantify the amplitude and runup of the waves induced by rotational cliff collapse, incorporating cliff fragmentation.

Along with the physical modeling, the wave generation and propagation phenomena have also been analyzed using While a few relevant studies provide partial understandings on the phenomena, such as as Liu et al. (2025) numerically analyzed the waves induced by different types of mass movements, considering different shapes using smoothed particles, similarly, Heller et al. (2021) experimentally analyzed the waves induced by iceburg calving and Yin et al. (2015) studied the potential cliff collapse of Jianchuandong rock mass in Three Gorges dam. While these studies contribute to the broader understanding of the impact induced by water waves, they do not consider the combined effect of rotational collapse and fragmentation. Moreover, the shape of the induced splash, as observed in Lake Furnas, has also not been properly explored either experimentally or numerically, as can be seen in Fig. 1 (a, b, and c), the falling cliff was still intact and broke under its own weight upon impact with the water surface and induced a huge splash.

Parallel advancements in numerical modeling by using have enhanced our understanding of landslide induced water waves thorugh, computational fluid dynamics (CFD), Eulerian and Lagrangian methods, employing depth-averaged model, nonlinear shallow water,

Formatted: Header

Formatted

Formatted

Formatted

Formatted

Formatted: Normal, Left, Indent: First line: 0.63 cm, Don't adjust right indent when grid is defined, Space Before: 0 pt, Line spacing: 1.5 lines, No bullets or numbering, Don't adjust space between Latin and Asian text, Don't adjust space between Asian text and numbers, Tab stops: Not at 5.87 ch

Formatted

Formatted

Navier-Stokes model, or Boussinesq equation, for both two- and three-dimensional modeling (Cecioni modelling (Franci et al., 20112020; Grilli et al., 2019; Guan and Shi, 2023; Heidarzadeh et al., 2020; Løvholt et al., 2005; Ruffini et al., 2019; Watts et al., 2003; Whittaker et al., 2017; Yavari and Ataie-Ashtiani, 2017). Moreover, numerous scientists have also used computational fluid dynamics (CFD) methods to analyze wave phenomena, just like experimental modeling, considering the sliding phase as solid material and water as the fluid phase (Abadie et al., 2010; Chen et al., 2020; Clous and Abadie, 2019; Franci et al., 2020b; Guan and Shi, 2023; Heller et al., 2016; Kim et al., 2020; Ma et al., 2015; Montagna et al., 2011; Mulligan et al., 2020; Paris et al., 2021; Rauter et al., 2022; Ruffini et al., 2019). Though these methods have successfully analysed the wave generation, propagation, and wave dynamics either induced by granular slide or block slide, their direct application to rotational cliff collapse remains limited. 2022; Romano et al.,

Formatted: Header

Formatted

Formatted

Formatted

Formatted

Formatted

Formatted

Formatted: Normal, Left, Indent: First line: 0.74 cm, Don't adjust right indent when grid is defined, Space Before: 0 pt, Line spacing: 1.5 lines, No bullets or numbering, Don't adjust space between Latin and Asian text, Don't adjust space between Asian text and numbers, Tab stops: Not at 5.87 ch

~~2020; Shi et al., 2016).~~

Furthermore, ~~scientists have also developed~~ empirical and regression-based hybrid prediction models have been developed for landslide-induced water waves by considering ~~a combination of several parameters, i.e.,~~ geometric, geological, and kinematic ~~characteristics of slides that contribute to wave generation~~parameters, as shown in Table 1. ~~Scientists have M. M.~~ Das and Wiegel (1972) proposed that the sliding velocity ~~of the sliding material~~ and water depth are the main ~~components~~ factors affecting the wave amplitude ~~of the waves.~~. Watts (1998) emphasised ~~Stated that~~ the role of slope angle, length, and mass ~~of the slide are major factors influencing the amplitude of the wave.~~, while Fritz et al. (2003) highlighted ~~stated that~~ the role of landslide mass thickness ~~mainly drives~~governing the amplitude of the induced wave. ~~The empirical relations mentioned in Table 1 are mainly for the landslide-induced water waves, not for cliff collapse-induced water waves. Since this study is related to the wave induced by rotational cliff collapse, not the granular slide, the contributing parameters should also be different. Here in this study, we have considered seven parameters for developing a prediction model, i.e., water depth, fall height of the cliff, number of fragments, runup slope angle, height of the cliff, and impact velocity. In this study, we have incorporated a new parameter, i.e., the number of fragments, as the induced waves from fragments better replicate actual geohazard events.~~

~~Since the experimental and numerical models are expensive, laborious, time-consuming, and require a lot of expertise, to overcome~~While these ~~problems, there is a need for~~ models ~~that are quick and require less effort and cost. Consequently, the use of AI~~provide important parameteric correlations, they were developed for translational or granular slides and show limited application for complex rotational cliff collapses involving fragmentation (Dai et al., 2023; Dignan et al., 2023; Esposti Ongaro et al., 2021).

~~and ML-based models is gaining fame in the field of engineering. Previous prediction models for wave amplitude and runup employ simple regression analysis, which is insufficient for complex problems involving multiple parameters, but recently~~Recently, scientists have shifted ~~towards more advanced ML models~~ to machine learning (ML) approaches for predicting wave dynamics (Bujak et al., 2023; Cesario et al., 2024; Li et al., 2024, ~~2023a~~2023; Romano et al., 2009; Tarwidi et al., 2023; Tian et al., 2025; Wang et al., ~~2017b~~2017; Wiguna, 2022). While these prediction models have shown improved performance over traditional regression and hybrid models, there is a need to develop an ML~~). Though scientists have used machine learning for wave amplitude and runup prediction modeling induced by various types of gravity flows, the prediction model for the waves induced by the rotational collapse of the cliff involving fragmentation is nonexistent to the authors' knowledge. Here in this study,~~

Formatted: Header

Formatted

Formatted: Font: (Default) Times New Roman, Font color: Red, Not Expanded by / Condensed by

Formatted

Formatted: Font: (Default) Times New Roman, Font color: Red, Not Expanded by / Condensed by

Formatted

Formatted

Formatted

Formatted

Formatted

Formatted

Formatted

Formatted

Formatted

Formatted

Formatted: Normal, Left, Indent: First line: 0.74 cm, Don't adjust right indent when grid is defined, Line spacing: 1.5 lines, No bullets or numbering, Don't adjust space between Latin and Asian text, Don't adjust space between Asian text and numbers, Tab stops: Not at 5.87 ch

Formatted: Font: (Default) Times New Roman, Font color: Red

Formatted: Font: (Default) Times New Roman, Font color: Red, Not Expanded by / Condensed by

Formatted

Formatted

Formatted

Formatted

~~we have developed prediction models for wave amplitude and runup using genetic programming (GP). GP-based~~ ~~models have recently gained traction for prediction, and multi-~~framework for predicting amplitude and runup of the waves induced by rotational cliff collapse, considering fragmentation.

~~expression programming~~To address this gap, the current study uses Genetic Programming (GP), and specifically Multi-Expression Programming (MEP) ~~and genetic-expression programming (GEP) are the most advanced, sophisticated, and widely used models. Both models are gene type programming models that form tree-like models. These models are~~), to develop a data-driven prediction model for the wave amplitude and runup. This model is similar to living organisms, which can learn, adapt, and modify their composition, size, and shape (Gardezi et al., 2024)~~.; Usama et al., 2023).~~ MEP is a cutting-edge, advanced form of ~~GEP~~ GP that adopts a demonstrative model for programming and uses linear chromosomes to determine optimum population size, mutation probability, and evolutionary model. Compared to other ML models, it can produce more precise results even when the problem complexity is unknown (Usama et al., 2023)~~).~~

In this study, we have experimentally and numerically analyzed the hydrodynamics of the wave induced by rotational cliff collapse, considering fragmentation of the cliff upon impact, and have also developed a prediction model for wave amplitude and runup. The physical modeling was carried out by developing a scaled water flume and a platform inducing rotational motion of the cliff. A total of 162 experiments were carried out ~~by~~, varying ~~the~~ seven control parameters~~,~~ ~~i.e.,~~: water depth, fall height, cliff mass, impact velocity, cliff height, runup slope angle, and number of fragments~~; for the sake of~~. To improve accuracy~~, each experiment was conducted twice, for~~ and consistency, ~~thus making it~~each parametric combination was averaged from two experimental values; hence, a total of 81 ~~experiments.~~experimental results were obtained. The parameters were selected to comprehensively elaborate on the distinct phases of rotational cliff collapse and induced waves. Water depth and runup slope angle provide the basis for wave propagation and runup. Whereas, the cliff collapse dynamics are explained by cliff mass (which governs the energy input), height of the cliff (defines the initial potential energy), and fall height (determines the transformation of potential to kinetic energy). Cliff impact velocity determines the amount of kinetic energy imparted to the water body at the time of impact, which is important for wave generation. Finally, the number of fragments is selected to demonstrate the effect of fragments of cliff upon impact with the water surface on wave amplitude and runup height. Together, these parameters define the energy budget from the state of rest to its release and then transfer to the water body to

Formatted: Header

Formatted

Formatted: Normal, Left, Indent: First line: 0.74 cm, Don't adjust right indent when grid is defined, Line spacing: 1.5 lines, No bullets or numbering, Don't adjust space between Latin and Asian text, Don't adjust space between Asian text and numbers, Tab stops: Not at 7.87 ch

Formatted

Formatted

Formatted

Formatted

Formatted

Formatted

Formatted

Formatted

Formatted

Formatted: Normal, Left, Indent: First line: 0.74 cm, Don't adjust right indent when grid is defined, Space Before: 0 pt, Line spacing: 1.5 lines, No bullets or numbering, Don't adjust space between Latin and Asian text, Don't adjust space between Asian text and numbers, Tab stops: Not at 5.87 ch

Formatted

Formatted

Formatted

Formatted

Formatted

Formatted

Formatted

Formatted

Formatted: Font: (Default) Times New Roman, Not Expanded by / Condensed by

Formatted

Formatted

Formatted

Formatted

Formatted

Formatted

Formatted

Formatted

Formatted

its final stage as amplitude and runup. Since the wave velocity was not directly measured during the experiments, it was measured using a 2D numerical model ~~was~~ developed using Ansys-Fluent~~, and wave velocity was measured; moreover~~. Furthermore, the numerical modeling results ~~from the experiment~~for wave amplitude and runup were ~~also~~ cross-validated~~.~~ with their experimental counterparts.

Finally, based on experimental results, prediction modeling for the amplitude and runup of water waves was carried out using multi-expression programming (MEP), and a novel prediction model was developed for the water waves induced by rotational cliff collapse, considering fragmentation of the cliff upon impact with the water surface.

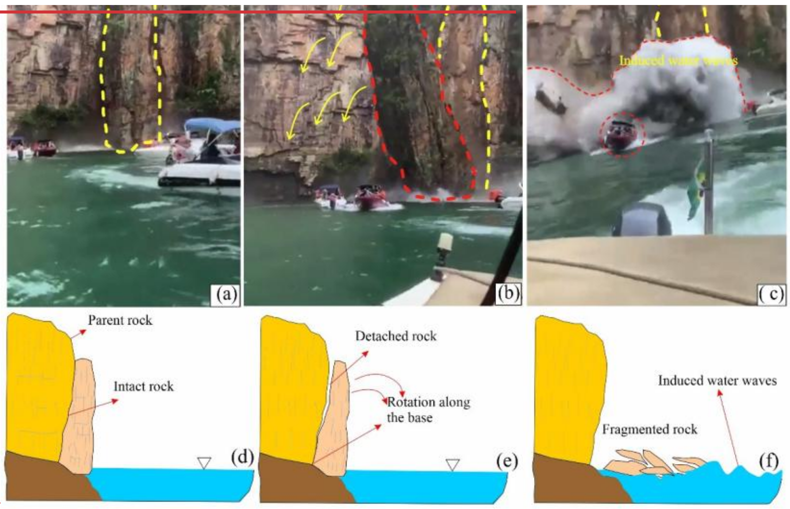

Formatted: Header

Formatted

Formatted

Formatted

Formatted: Font: (Default) Times New Roman, Font color: Red, Not Expanded by / Condensed by

Formatted: Font: (Default) Times New Roman

Formatted: Normal, Left, Indent: First line: 0.74 cm, Space Before: 0 pt, Line spacing: 1.5 lines, No bullets or numbering, Tab stops: Not at 5.87 ch

Formatted

Formatted

Formatted

Formatted

Formatted: Normal, Left, Indent: First line: 0.74 cm, Space Before: 0 pt, Line spacing: 1.5 lines, No bullets or numbering, Tab stops: Not at 5.87 ch

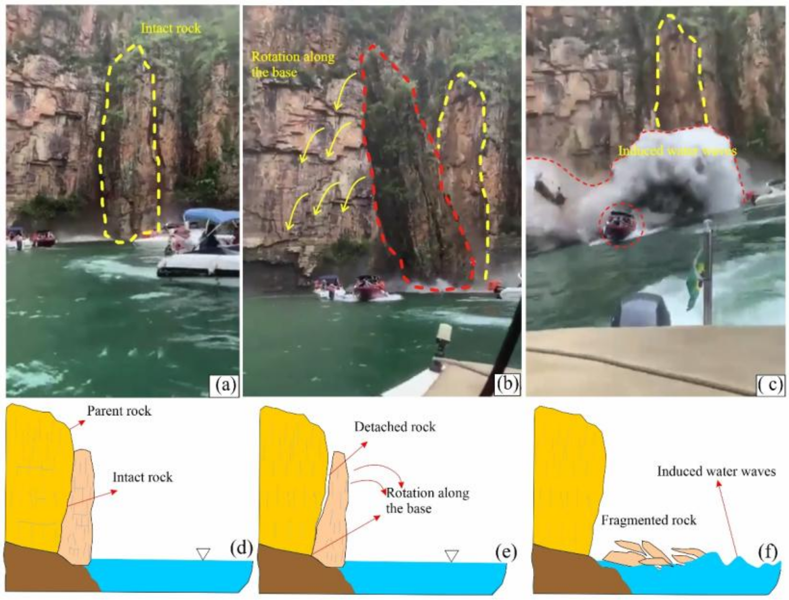

Fig. 1: (a, b, and c) waves induced by a cliff collapse in Lake Furnas, Brazil. (d, e, and f) sketch diagram indicating the detachment and rotational fall process.

Table 1: Historical overview of the prediction models for wave amplitude

Authors	Predictive model
Kamphuis and Bowering	v_s 0.7 l_s

Formatted: Header
Formatted
Formatted
Formatted: Normal, Centered, Don't adjust right indent when grid is defined, Line spacing: single, No bullets or numbering, Don't adjust space between Latin and Asian text, Don't adjust space between Asian text and numbers, Tab stops: Not at 9.4 ch
Formatted: Font: (Default) Times New Roman
Formatted
Formatted: Normal, Left, Don't adjust right indent when grid is defined, Space After: 0 pt, Line spacing: 1.5 lines, No bullets or numbering, Don't adjust space between Latin and Asian text, Don't adjust space between Asian text and numbers, Tab stops: Not at 5.87 ch
Formatted: Font: (Asian) +Body Asian (等线), 8 pt, Not Expanded by / Condensed by
Formatted: Font: 8 pt
Formatted: Font: (Asian) +Body Asian (等线), 8 pt, Not Expanded by / Condensed by
Formatted: Font: 8 pt
Formatted: Normal, Centered, Indent: Left: 0 cm, Space Before: 0 pt
Formatted Table
Formatted

(, 1970)	$A_m = \left(\frac{v_s}{\sqrt{gh}}\right)^{0.7}\left(0.31 + 0.2\log\left(\frac{l_s}{h^2}\right)\right) + 0.35e^{-0.08(x/h)}$
(Noda, 1970)	$A_m = 1.32\frac{v_s}{\sqrt{gh}}$
(Huber and Hager, 1997)	$\frac{H_m}{h} = 2\times 0.88\sin\theta\cos^2\left(\frac{2\alpha}{3}\right)\left(\frac{\rho_s}{\rho_w}\right)^{0.25}\left(\frac{V}{wh^2}\right)^{0.5}\left(\frac{r}{h}\right)^{-\frac{2}{3}}$
(Fritz et al., 2004)	$A_m = 0.25\left(\frac{v_s}{\sqrt{g_h}}\right)^{1.4}\left(\frac{s}{h}\right)^{0.8}$
(Panizzo et al., 2005)	$\frac{H_m}{h} = 0.07\left(\frac{T_s h^2}{ws}\right)^{-0.45}(\sin\alpha)^{-0.88}e^{0.6\cos\theta}\left(\frac{r}{n}\right)^{-0.44}$
(Heller, 2007)	$A_m = \frac{4}{9}\left[F\left(\frac{s}{h}\right)^{1/2}\rho^{1/4}\left(\cos\frac{6\alpha}{7}\right)^2\right]^{4/5}$
(Mohammed and Fritz, 2012)	$A_m = max(A_{C_1}, A_{C2})$ $A_{c1} = 0.3F^{2.1}\left(\frac{s}{h}\right)^{0.6}\left(\frac{r}{h}\right)^{\left(-1.2F^{0.25}\left(\frac{s}{h}\right)^{-0.02}w-0.33/h\right)}\cos\alpha$ $A_{c2} = 1.0FS^{0.8}\left(\frac{w}{h}\right)^{-0.4}\left(\frac{l}{h}\right)^{-0.5}\left(\frac{\gamma}{h}\right)^{-1.5F^{0.5}\left(\frac{w}{h}\right)^{-0.07}\left(\frac{w}{h}\right)^{-0.3}}\cos^2\alpha$
(Wang et al., 2016)	$A_m = 1.17F\left(\frac{sl}{bh}\right)^{0.25}\left(\frac{w}{b}\right)^{0.45}(\sin^2\alpha + 0.6\cos^2\alpha)$
(Li et al., 2023)	$A_m = 0.59\sqrt{\frac{2H(1-f\cot\alpha)}{h}}\left(\frac{swl}{h^3}\right)^{N-0.11}\left(\frac{x}{h}\right)^{-0.43}\cos^2\left(\frac{2}{3}\alpha\right)$

Note: *l* is the landslide length; *s* is the landslide thickness; *w* is the landslide width; m is the landslide mass weight; *V* is the landslide volume; *H* is the landslide height; T_s time for motion of slide, *b* is the river width; *h* is the still water depth; *x*(*r*) is the offshore distance from the bank slope; *α* is the slope angle; *θ* is the angular direction; v_s is the impact velocity.

Fritz et al. (2004)	$A_m = 0.25\left(\frac{v_s}{\sqrt{g_h}}\right)^{1.4}\left(\frac{s}{h}\right)^{0.8}$
Panizzo et al. (2005)	$\frac{Hm}{h} = 0.07\left(\frac{T_s h^2}{ws}\right)^{-0.45}(\sin\alpha)^{-0.88}e^{0.6\cos\theta}\left(\frac{r}{n}\right)^{-0.44}$
Heller (2007)	$A_m = \frac{4}{9}\left[F\left(\frac{s}{h}\right)^{1/2}\rho^{1/4}\left(\cos\frac{6\alpha}{7}\right)^2\right]^{4/5}$
Mohammed and Fritz (2012)	$A_m = max(A_{c1}, A_{c2})$ $A_{c1} = 0.3F^{2.1}\left(\frac{s}{h}\right)^{0.6}\left(\frac{r}{h}\right)^{\left(-1.2F^{0.25}\left(\frac{s}{h}\right)^{-0.02}w-0.33/h\right)}\cos\alpha$ $A_{c2} = 1.0FS^{0.8}\left(\frac{w}{h}\right)^{-0.4}\left(\frac{l}{h}\right)^{-0.5}\left(\frac{\gamma}{h}\right)^{-1.5F^{0.5}\left(\frac{w}{h}\right)^{-0.07}\left(\frac{w}{h}\right)^{-0.3}}\cos^2\alpha$
Wang et al. (2016)	$A_m = 1.17F\left(\frac{sl}{bh}\right)^{0.25}\left(\frac{w}{b}\right)^{0.45}(\sin^2\alpha + 0.6\cos^2\alpha)$
Li et al. (2023)	$A_m = 0.59\sqrt{\frac{2H(1-f\cot\alpha)}{h}}\left(\frac{swl}{h^3}\right)^{N-0.11}\left(\frac{x}{h}\right)^{-0.43}\cos^2\left(\frac{2}{3}\alpha\right)$
Note: *Note*: *l* is the landslide length; *s* is the landslide thickness; *w* is the landslide width; m is the landslide mass weight; *V* is the landslide volume; *H* is the landslide height; *b* is the river width; *h* is the still water depth; *x*(*r*) is the offshore distance from the bank slope; *α* is the slope angle; *θ* is the angular direction; *vs* is the impact velocity.	

2. 2. Research methodology

2.1 Model Preparation Experimental setup

The physical modeling for wave amplitude and runup induced by rotational cliff

Formatted: Header
Formatted
Formatted: Normal, Centered, Indent: Left: 0 cm, Right: 0 cm, Space Before: 0 pt
Formatted: Font: Times New Roman, 8 pt, Not Raised by / Lowered by
Formatted: Normal, Centered, Indent: Left: 0 cm, Line spacing: single, Tab stops: Not at 16.28 ch
Formatted
Formatted: Normal, Centered, Indent: Left: 0 cm, Right: 0 cm, Space Before: 0 pt
Formatted: Font: Times New Roman, 8 pt
Formatted: Normal, Centered, Indent: Left: 0 cm, Line spacing: single, Tab stops: Not at 15.33 ch
Formatted
Formatted: Normal, Centered, Indent: Left: 0 cm, Right: 0 cm, Space Before: 0 pt
Formatted: Font: Times New Roman, 8 pt
Formatted: Normal, Centered, Indent: Left: 0 cm, Line spacing: single, Tab stops: Not at 14.01 ch + 15.94 ch + 19.48 ch + 23.22 ch
Formatted
Formatted: List Paragraph, Left, Don't adjust right indent when grid is defined, Space Before: 0.5 line, Line spacing: 1.5 lines, Outline numbered + Level: 1 + Numbering Style: 1, 2, 3, … + Start at: 1 + Alignment: Left + Aligned at: 0 cm + Indent at: 0.63 cm, Don't adjust space between Latin and Asian text, Don't adjust space between Asian text and numbers, Tab stops: Not at 5.87 ch
Formatted
Formatted

collapse was carried out in a three-dimensional water flume made up of plexiglass, as shown in Figs. 2 and 3. One end of the flume is vertical at 90°, whereas the other end is inclined and fixed at 30° (Fig. 3a and b). The flume is 0.55 m high, 0.5 m wide, and 1.4 m long along the base and 2.35 m long at the top. Furthermore, to measure the runup of induced water waves at various slope angles, two sliding rails were installed towards the inclined end at 45° and 60°. So, upon insertion of the gate at 45°and 60°, the top length of the flume was further reduced according to the Pythagoras theorem. To induce the rotational cliff collapse, a 0.55 m wide and 0.6 m high movable platform was ~~prepared~~ designed, which can move in the vertical direction and can also rotate about its axis.

The rotational motion was induced by pulling the hinge; the release ensured a pure rotational motion, which was visually verified by video analysis. The flume was marked with a vertical scale to measure the water depth. The wave amplitude was measured using capacitance-type wave gauges with an accuracy of ± 0.5 mm, placed along the centerline at specified intervals. The runup height was measured using a graduated paper attached to the inclined surface. The entire process was recorded using a digital camera (240 fps, 720p resolution) placed perpendicular to the experimental flume; the velocity of the falling cliff was verified by frame-by-frame video analysis using Particle Image Velocitymeter (PIV).

Formatted: Header

Formatted

Formatted

Formatted

Formatted

Formatted

Formatted

Formatted

Formatted

Formatted

Formatted: Normal, Left, Indent: First line: 0.63 cm, Don't adjust right indent when grid is defined, Line spacing: 1.5 lines, No bullets or numbering, Don't adjust space between Latin and Asian text, Don't adjust space between Asian text and numbers, Tab stops: Not at 5.87 ch

Formatted

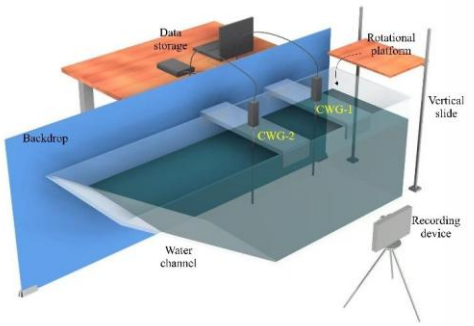

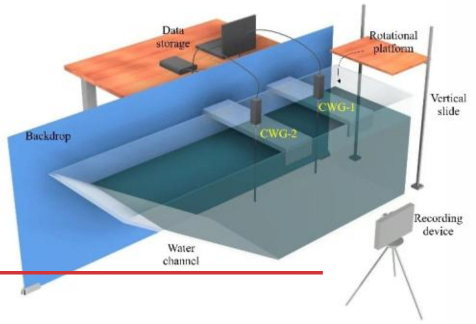

Fig. 2: Illustration of experimental setup including wave gauges, rotational platform, recording, and data storage devices.

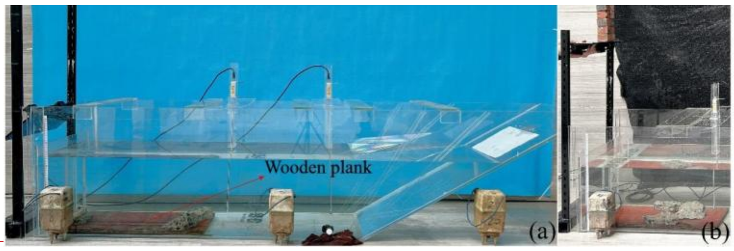

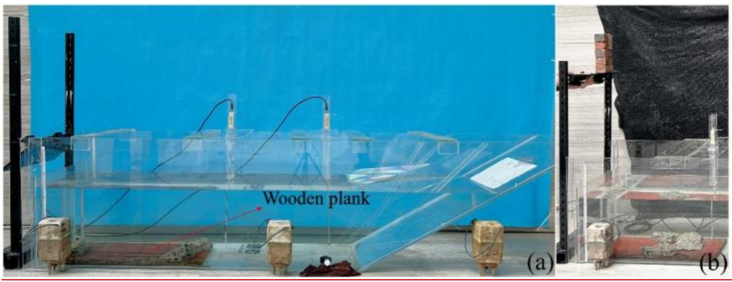

Fig. 3: Photographs of the setup, (a) Experimental flume, (b) platform for inducing rotational cliff collapse.

2.2 Test preparation and materials

Physical experiments were carried out by varying the water depth, fall height,

Formatted: Header

Formatted

Formatted

Formatted: Normal, Centered, Don't adjust right indent when grid is defined, Space Before: 0 pt, Line spacing: 1.5 lines, No bullets or numbering, Don't adjust space between Latin and Asian text, Don't adjust space between Asian text and numbers, Tab stops: Not at 17.46 ch

Formatted

Formatted

Formatted: Normal, Centered, Don't adjust right indent when grid is defined, Line spacing: single, No bullets or numbering, Don't adjust space between Latin and Asian text, Don't adjust space between Asian text and numbers, Tab stops: Not at 20.22 ch

Formatted

Formatted

number of fragments, bank slope angle, mass of falling rock, cliff height, and impact velocity. The tests were carried out for three water depths, i.e., 0.34 m, 0.27 m, and 0.20 m, and three fall heights, i.e., 0.64 m, 0.44 m, and 0.245 m from the surface of the water ~~level~~. Furthermore, the number of blocks was also varied, i.e., 6, 10, and 12 blocks having combined weights of 1.445 kg, 2.29 kg, and 2.82 kg, respectively. At the same time, the impact velocity changed by changing the fall height. The wave runup was measured by varying the bank slope angle, i.e., 30°, 45°, and 60°.

To replicate the field density of the rocks, red gutka bricks having a density of around 2000 kg/m^3 were used. ~~The single~~A singular block had a dimension of 0.~~55~~055x0.05x0.042

Formatted: Header

Formatted

Formatted

Formatted

Formatted

Formatted

Formatted

Formatted

Formatted: Normal, Indent: First line: 0.74 cm, Don't adjust right indent when grid is defined, Line spacing: 1.5 lines, No bullets or numbering, Don't adjust space between Latin and Asian text, Don't adjust space between Asian text and numbers, Tab stops: Not at 5.87 ch

Formatted

Formatted

m. The mass volume and dimension of all the blocks were unchanged to ensure consistency in the experiments. A combination of 6, 10, and 12 blocks of red gutka bricks was used to form a cliff and measure the wave amplitude and runup of induced waves. The blocks were joined together with the help of cement paste having a water-cement ratio W/C 0.8 and cured for 2 hours in front of an electric heater at 150 °C. To ensure the weak bond strength, several trials for bond strength were carried out after a curing period of 2 hours, and it was found to be in the range of 0.42-0.5 MPa. In contrast, the inertial stresses at the time of impact were several times higher, such that they caused the fragmentation of the cliff. This condition was purposely designed to imitate naturally fractured cliff materials, confirming that the structure fragmented primarily along the joints upon impact with the water surface, consistent with field observations of rotational cliff collapses. The bonded blocks were placed on the rotational platform at specific heights, i.e., 0.64 m, 0.44 m, and 0.245 m from the water level, and were allowed to rotate under their own weight by pulling the hinge, such that the placed block falls in the water following rotation motion along its base Fig. 3 (b). To avoid the slippage of blocks and to ensure that it had sufficient frictional resistance needed for pure rotational motion of the simulated cliff, finely-grounded bricks of the same cliff material were pasted on the rotational platform, thereby preventing translational motion or vertical free fall into the water.

Furthermore, to reduce the impact of falling blocks on the base of the flume, a wooden plank weighing 2.69 kg and dimensions 0.65mx0.37mx0.01 m was placed at the point of impact inside the flume. Due to its large surface area and lighter density, it tends to float in the flume, so two blocks of concrete weighing 3.58 kg were placed on it, Fig. 3 (a). Since the fall height was small, no considerable local breakage was observed in the blocks, and the brief water contact minimised the water absorption effect.

The induced wave amplitude was measured by placing the wave measuring gauges at a distance of 0.65 m and 0.135 m from the vertical face; the gauges were wired and connected to the laptop. At the same time, the runup was measured manually with the help of a scale by pasting a scaled paper on the slope. Furthermore, the experiments were also recorded with the help of a high-resolution camera for verification purposes.

2.3 Numerical Modeling

Simulating multi-phase flows is challenging due to the constant deformation of the liquid-gas interface. Various numerical methods have been developed to model these flows, each offering unique advantages depending on the specific flow regime and characteristics of interest. In this study, the Volume of Fluid (VOF) method is utilized for its effectiveness in handling significant interface distortions and topological changes. The VOF method offers superior mass conservation, which is critical in high velocity _impact conditions where liquid fragmentation and wave generation are significant (Brackbill (Backbill et al., 1992; Hirt and Nichols, 1981). Alternative numerical schemes, such as the Front Tracking approach, are generally limited). Other approaches provide superior

Formatted: Header

Formatted: Font: (Default) Times New Roman

Formatted: Font: (Default) Times New Roman, Not Expanded by / Condensed by

Formatted: Font: (Default) Times New Roman

Formatted: Font: (Default) Times New Roman, Not Expanded by / Condensed by

Formatted: Font: (Default) Times New Roman

Formatted: Font: (Default) Times New Roman, Not Expanded by / Condensed by

Formatted: Font: (Default) Times New Roman

Formatted: Font: (Default) Times New Roman, Not Expanded by / Condensed by

Formatted: Font: (Default) Times New Roman

Formatted: Font: (Default) Times New Roman, Not Expanded by / Condensed by

Formatted: Font: (Default) Times New Roman

Formatted: Font: (Default) Times New Roman, Not Expanded by / Condensed by

Formatted: Font: (Default) Times New Roman

Formatted: Font: (Default) Times New Roman, Not Expanded by / Condensed by

Formatted: Font: (Default) Times New Roman

Formatted: Font: (Default) Times New Roman, Not Expanded by / Condensed by

Formatted: Font: (Default) Times New Roman

Formatted: Font: (Default) Times New Roman, Not Expanded by / Condensed by

Formatted: Font: (Default) Times New Roman, Font color: Black, Not Expanded by / Condensed by

Formatted: Font: (Default) Times New Roman, Font color: Black

Formatted: Font: (Default) Times New Roman, Font color: Black, Not Expanded by / Condensed by

Formatted: Font: (Default) Times New Roman, Font color: Black

Formatted: Font: (Default) Times New Roman, Font color: Black, Not Expanded by / Condensed by

Formatted: Font: (Default) Times New Roman, Font color: Black

Formatted: Font: (Default) Times New Roman, Font color: Black, Not Expanded by / Condensed by

Formatted: Font: (Default) Times New Roman, Font color: Black

Formatted: Font: (Default) Times New Roman, Font color: Black, Not Expanded by / Condensed by

Formatted: Font: (Default) Times New Roman, Font color: Black

Formatted: Font: (Default) Times New Roman, Font color: Black, Not Expanded by / Condensed by

Formatted: Font: (Default) Times New Roman, Font color: Black

Formatted: Font: (Default) Times New Roman, Font color: Black, Not Expanded by / Condensed by

Formatted: Font: (Default) Times New Roman, Font color: Black accuracy in modeling interfaces and surface tension, but they struggle to managehandling complex scenarios (topological changes (Tryggvason et al., 2001; Liu and Liu, 2010; Monaghan, 1994; Yang and Kong, 2018). Another approach is the Level Set method, but it suffers from mass conservation and convergence issues. The Lattice Boltzmann Method (LBM) is also common; however, its applicability to high velocity impact is rather limited (Aidun & Clausen, 2010). Given these trade-offs, the Volume of Fluid (VOF) method finds an optimal balance of computational efficiency, interface tracking capability, and proven reliability for modeling multiphase flow in the moderate-to-high velocity range relevant to this study. Therefore, a two-dimensional numerical model of a cliff, having the same properties as the experimental cliff mentioned previously, hitting the water surface is developed using the VOF method to accurately capture the liquid-gas interface.

In this approach, a volume fraction (α), ranging between 0 and 1, is applied across the entire computational domain. A value of α = 1 indicates a control volume filled with liquid, while α = 0 denotes a control volume filled with gas. The interface is represented by values where 0 < α < 1. In the Volume of Fluid (VOF) method, the momentum equation is solved across the entire computational domain, with the resulting velocity field shared by all phases. To account for surface tension effects, a continuum surface force (CSF) model is employed (Backbill et al., 1992).). The normal vector n n and interface mean curvature k are as follows, respectively:

interface mean curvature κ are as follows, respectively:

$$n = \frac{\nabla\alpha}{|\nabla\alpha|} \qquad (1)$$

$$n = \frac{\nabla\alpha}{|\nabla\alpha|} \qquad (1)$$

and

$$\kappa = \nabla \cdot \frac{\nabla\alpha}{|\nabla\alpha|} \qquad (2)$$

$$k = \nabla \cdot \frac{\nabla\alpha}{|\nabla\alpha|} \qquad (2)$$

The interface is maintained as sharp through the use of geometric reconstruction to ensure its clarity. The volume fraction (α) is discretizeddiscretised with the geo-reconstruct scheme, while the convective terms in the momentum equation are handled using a second-order upwind method. The PISO (Pressure-Implicit with Splitting of Operators) algorithm was employed for pressure-velocity coupling, which is well-suited for transient flows. Temporal discretizationdiscretisation employs a second-order implicit scheme, and spatial gradients are calculated using the Least Squares Cell-Based method.

To have anThe boundary conditions were defined as follows: the bottom boundary was modeled as a no-slip wall, while the top boundary was set as a pressure outlet at atmospheric conditions, and the lateral sides were modeled as stationary walls to

Formatted: Header

Formatted

Formatted

Formatted

Formatted

Formatted

Formatted

Formatted: Font: (Default) Times New Roman, 小四, Not Expanded by / Condensed by

Formatted: Normal, Indent: Left: 0 cm, Space Before: 0 pt, Line spacing: 1.5 lines

Formatted: Font: (Default) Times New Roman, 小四

Formatted

Formatted: Normal, Left, Indent: Left: 0 cm, Right: 0 cm, Space Before: 0 pt, Line spacing: 1.5 lines confine the liquid film within the domain. For accurate simulation of the rotational motion of the cliff through the air--water interface in a multi-phase flow environment, dynamic meshing was implemented within the ANSYS Fluent framework. This approach facilitated the adaptation of the computational mesh to accommodate the cliff's movement while maintaining the integrity of the liquid-gas interface captured by the Volume of Fluid (VOF) method. Dynamic meshing was critical for modeling the complex interactions between the falling cliff and the surrounding air and water phases, allowing the mesh to deform and adapt in response to the cliff's trajectory. In ANSYS Fluent, the dynamic meshing strategy employed a combination of mesh deformation and local remeshing techniques to handle the cliff's motion. Mesh deformation was applied to adjust the existing mesh nodes smoothly as the cliff moved, preserving mesh quality in regions experiencing moderate displacement. For areas near the cliff where significant deformation could lead to poor mesh quality, local remeshing was utilized to regenerate mesh elements for better numerical stability and accuracy. The smoothing and remeshing algorithms were configured to maintain high mesh quality, with a skewness threshold set to prevent excessive element distortion.

The rotational cliff collapse was simulated using an in-house user-defined function (UDF). This UDF interfaced with ANSYS Fluent to dynamically update the rock's position and velocity. To enhance computational efficiency, a dynamic mesh zone was defined around the cliff, with a finer mesh resolution near its surface to capture the sharp gradients in the flow field and interface dynamics. The mesh was gradually coarsened away from the rock to reduce computational cost while maintaining sufficient resolution in the far-field regions. The dynamic meshing process was synchronized synchronised with the transient flow solver, using a time step size determined through a time step independence study to balance accuracy and computational efficiency. It is also worth mentioning that the numerical simulations were performed considering the rock as a unified mass. This approach describes the slight differences between the experimental and numerical results, which are nonetheless within the acceptable range.

2.4 Multi-expression programming

The MEP model was developed for predicting wave amplitude and runup using experimental data, as shown in Table 2. A dataset of 81 experiments was prepared by alternately varying seven different parameters, and the results for wave amplitude and runup were recorded. experimental results was used as an input to a machine learning model. Furthermore, the data was divided into 70/30 ratios for training and validation purposes before developing the model. The model starts working by generating a random chromosome population, and it continues to generate the chromosomes until a terminal condition is achieved, generating an optimal expression from the data having input and output pairs over a certain number of generations, as shown in Fig. 4.

Based on a binary tournament process, parents are selected and then undergo a recombination process through a consistent crossover probability. This recombination produces two more offspring. These offspring go through mutation, and if these offspring perform better than the least fitting offspring in the current population, then the better offspring replace them. The illustrations used by MEP are similar to the ones used by C++ and Pascal compilers. The MEP chromosomes are comprised of numerous genes combined using various mathematical operators such as addition (+), subtraction (-), multiplication (x), and division (/), and these genes create expression trees (ETs) (Cheng et al., 2020). Moreover, there are several ~~parameters~~hyperparameters such as code length, sub-population size and number, crossover probability, and other sets of various functions involved in in generation of MEP code, and they also govern the overall performance of the code. Among these parameters, the size of the population tells us about the number of programs being generated, whereas an increase or decrease in subpopulation size directly affects the complexity and computation time of the model. Moreover, the length of the developed model is controlled by varying the code length parameter. During model development, prerequisite tuning procedures were applied to optimize these hyperparameters. This careful selection minimized the risk of premature convergence or underfitting while ensuring computational efficiency.

Table 2: ~~Input parameters~~Experimental dataset used for training and ~~corresponding wave amplitude and runup heights~~validation of the machine learning model.

S/No.	Water depth (d) (m)	~~Drop~~Fall height (H) (m)	Fragments (N_f)	Angle (α) (°)	~~Mass(m~~ Cliff Mass m (Kg)	Cliff height (h) (m)	Velocity (v) (m/s)	Amplitude (A) (m)	Runup R (m)
1	0.34	0.245	6	30	1.445	0.12	2.19	0.0225	0.051
2	0.34	0.445	6	30	1.445	0.12	2.95	0.0230	0.056
3	0.34	0.645	6	30	1.445	0.12	3.56	0.0365	0.068
4	0.34	0.245	6	45	1.445	0.12	2.19	0.0370	0.045
5	0.34	0.445	6	45	1.445	0.12	2.95	0.0425	0.051
37	0.27	0.245	10	30	2.295	0.20	2.19	0.0431	0.116
38	0.27	0.445	10	30	2.295	0.20	2.95	0.0510	0.129
39	0.27	0.645	10	30	2.295	0.20	3.56	0.0685	0.141
40	0.27	0.245	10	45	2.295	0.20	2.19	0.0390	0.085
41	0.27	0.445	10	45	2.295	0.20	2.95	0.0523	0.102

78	0.2	0.645	12	45	2.82	0.24	3.56	0.0733	0.146
79	0.2	0.245	12	60	2.82	0.24	2.19	0.0565	0.062
80	0.2	0.445	12	60	2.82	0.24	2.95	0.0636	0.083
81	0.2	0.645	12	60	2.82	0.24	3.56	0.0657	0.098

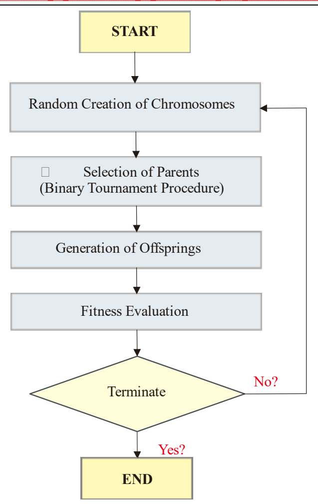

Fig. 4 Schematic representation of MEP workflow used in this study

3.1 Experimental results

3. Results and discussions

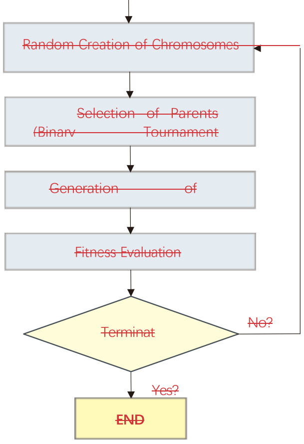

Fig. 4 MEP flowchart

The experimental results of the wave amplitude and runup, induced by rotational cliff collapse, reveal complex hydrodynamic processes. As shown in Fig. 5, the failure is initiated by the rotational fall of the cliff, leading to a significant amount of impact energy upon hitting the water surface. The impact induced a huge splash, which is evident from Fig. 5 (b, e & h). It was observed that the shape of the splash also varies with water depth for all the cases; higher water depths resulted in a mushroom-shaped splash, i.e., broader on the top, as the momentum dissipates before interacting with the bottom surface, resulting in a vertical jet and the formation of a mushroom-shaped splash. as can be seen in Fig. 5(h). The observed phenomena perfectly align with the basic concepts of fluid dynamics, which state that greater depths absorb more impact energy compared to shallow waters. Shallow waters produced a vertically elongated splash as can be seen in Fig. 5 (b & e). It can be observed that as the depth decreases, the splash becomes more elongated, and this is due to the fact that as shallower depths intensify the upward momentum transfer, thus resulting in a more

Formatted: Header
Formatted: Font color: Red
Formatted
Formatted
Formatted
Formatted
Formatted
Formatted
Formatted
Formatted: Font: (Default) Times New Roman, (Asian) +Body Asian (等线), Not Expanded by / Condensed by
Formatted
Formatted
Formatted
Formatted

elongated shape (Kubota and Mochizuki, 2009). ~~).~~

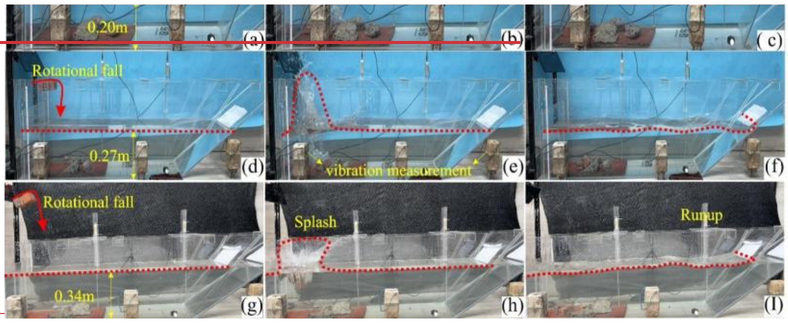

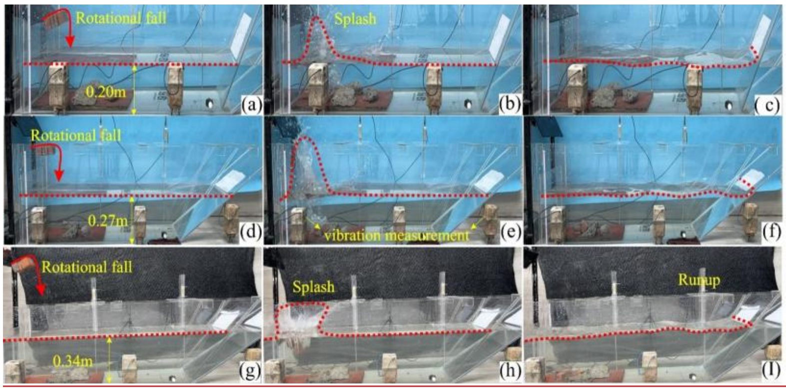

Fig. 5: A pictorial display of the experimental setup for various water depths, i.e., 0.20 m, 0.27m, and 0.34 m. (a, d & g) indicate rotational fall of the cliff, (b, e & h) showing splash as a result of cliff impact, (c, f & I) formation and propagation of induced wave and runup at various slope angles.

3.1.1 Relation between energy and amplitude

Further, the relationship between impact energy and wave response was also investigated by establishing a dimensionless impact energy parameter (K.E/ρgh³). Where *K.E* is the kinetic energy of the cliff, *ρ* is the density, and *h* is the water depth. The negative quadratic coefficient in Fig. 6(a) indicates a nonlinear response, such that at the start, the wave amplitude increases as the impact energy increases, but later it decreases, due to reduced energy transfer at higher impact values. At higher impact values, the released energy was not fully used in the wave formation and propagation; instead, a part of the energy was dissipated in the formation of splash, and in the formation of air pockets and their subsequent collapse. Moreover, the coefficient of determination was found to be 77% indicating a good data fit.

~~Moreover, the~~The results for the relative wave amplitude and wave energy were analyzed for three water depths, i.e., 0.34 m, 0.27 m, and 0.20 m., as shown in Fig. 6(b).

The results indicate a strong correlation for all three cases, with coefficients of determination around 0.96. The results indicate a direct relation between wave height and energy, whereas the decreasing slope values with the increasing water depth suggest that for deeper water the wave amplitude decreases at a slower rate with increasing wave energy, thus highlighting the impact of water depth on the wave dynamics, such that shallower water allows more amplification of waves for the same energy level, and this is due to the increased non-linear interactions and enhanced energy concentrations in shallower depths (Myrhaug and Lader, 2019).).

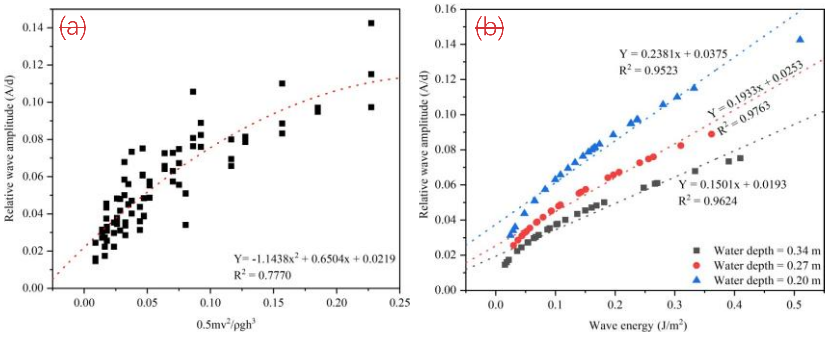

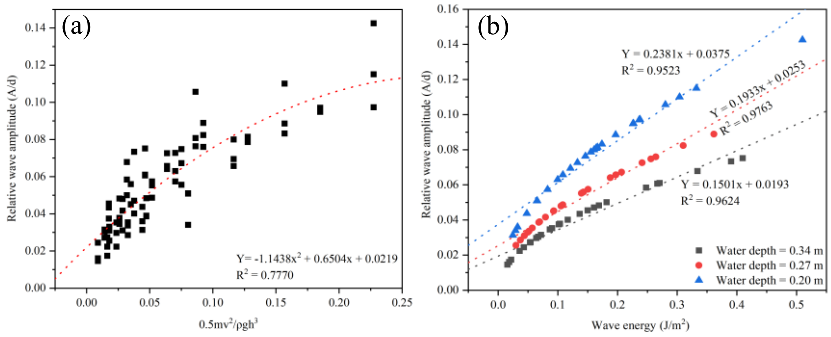

Fig. 6: (a) ImpactDimensionless impact energy (K.E/ρgh³) vs relative wave amplitude, indicating a nonlinear trend. (b) Wave energy vs relative wave amplitude

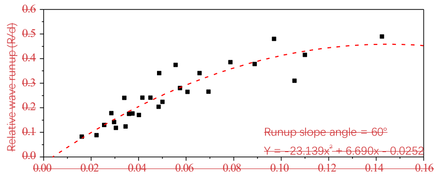

Relative wave amplitude (A/d)

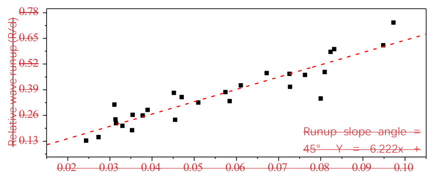

Relative indicating higher wave amplitude (A/d) amplifications in shallow waters.

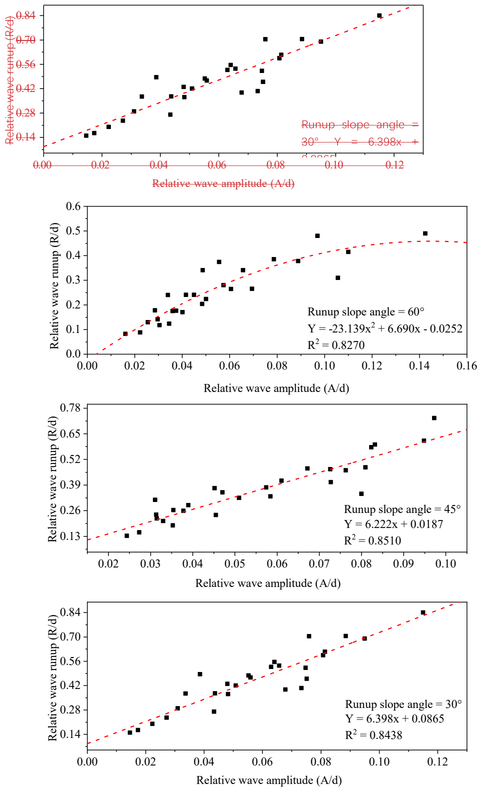

Fig. 7: Relative wave amplitude vs relative wave heightrunup at various slope angles and water depth.

The results for the relative wave height and runup for all three water depths and three runup slope angles are shown in Fig. 7. The relationship indicates a strong correlation between wave amplitude and runup for all three slope angles. TheThe decreasing line-slope values with increasing runup slope angle indicate that wave runup increases at a slower rate for sharp slope angles compared to mild slopes. The trend highlights the effect of slope angle on the runup. The result also indicates that the mild slope angles help wave runup amplification, as they dissipate a very small amount of energy, whereas steeper angles result in lower runup heights because of higher energy losses (Wu et al., 2018).

Formatted: Header
Formatted: Font: (Default) Times New Roman, Font color: Red
Formatted: Font: (Default) Times New Roman, Font color: Red, Not Expanded by / Condensed by
Formatted: Font: (Default) Times New Roman, Font color: Red
Formatted: Font: (Default) Times New Roman, Font color: Red, Not Expanded by / Condensed by
Formatted: Font: (Default) Times New Roman, Font color: Red
Formatted: Font: (Default) Times New Roman, Font color: Red, Not Expanded by / Condensed by
Formatted: Font: (Default) Times New Roman, Font color: Red
Formatted: Font: (Default) Times New Roman, Font color: Red, Not Expanded by / Condensed by
Formatted: Font: (Default) Times New Roman, Font color: Red
Formatted: Font: (Default) Times New Roman, Font color: Red, Not Expanded by / Condensed by
Formatted: Font: (Default) Times New Roman, Font color: Red
Formatted ...
Formatted ...
Formatted ...
Formatted ...
Formatted ...
Formatted ...
Formatted ...
Formatted ...
Formatted: Font: (Default) Times New Roman, 小四
Formatted ...
Formatted: Font: (Default) Times New Roman, 小四
Formatted ...
Formatted: Font: (Default) Times New Roman, 小四
Formatted ...
Formatted: Font: (Default) Times New Roman, 小四
Formatted ...
Formatted: Font: (Default) Times New Roman, 小四
Formatted ...
Formatted: Font: (Default) Times New Roman, 小四
Formatted ...
Formatted: Font: (Default) Times New Roman, 小四
Formatted ...
Formatted: Font: (Default) Times New Roman, 小四
Formatted ...
Formatted: Font: (Default) Times New Roman, 小四
Formatted ...
Formatted: Font: (Default) Times New Roman, 小四
Formatted ...

decreasing line-slope values with increasing runup slope angle indicate that wave runup increases at a slower rate for sharp slope angles compared to mild slopes. The trend highlights the effect of slope angle on the runup. The result also indicates that the mild slope angles help wave runup amplification, as they dissipate a very small amount of energy, whereas steeper angles result in lower runup heights because of higher energy losses (Wu et al., 2018).

3.1.2 Impact Froude no vs Relative wave amplitude

Fig. 8 indicates the relationship between the impact Froude number and relative wave amplitude (A/d), under varying experimental conditions for the first gauge, i.e., near the impact zone. Since we are interested in the immediate response of the wave influenced by the impact Froude number. The results indicate that as the water depth decreases, the relative wave amplitude and impact Froude number increase, indicating a reduction in the dissipation of impact energy, causing pronounced surface turbulence and increased wave height. Additionally, the decreased water depth also increased the value of the impact Froude number by reducing its characteristic velocity, resulting in stronger wave generation upon impact. The calculations for Reynolds number for the experiments resulted in very high values, thus indicating a strong turbulent flow, which is also evident from Fig. 5, so viscous effects are very, very small and can be ignored, thus indicating the Froude dynamics similarity. The experimental results indicate the complex interaction between wave propagation, impact dynamics, and bathymetrical effects in waves induced by rotational cliff collapse. Moreover, upon impact, the cliff fragmentation distributes impact energy over a larger area of water, thus increasing wave height by enhanced turbulence and water splashing effects.

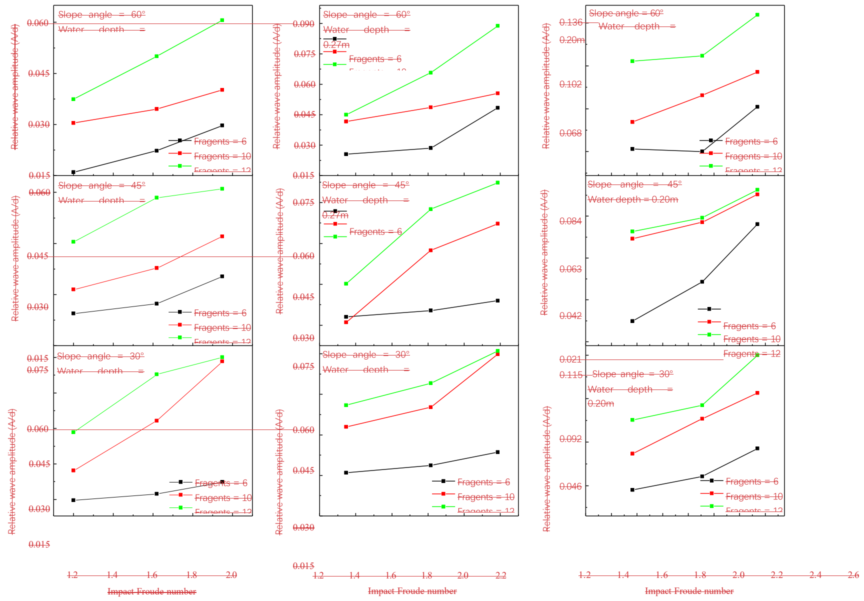

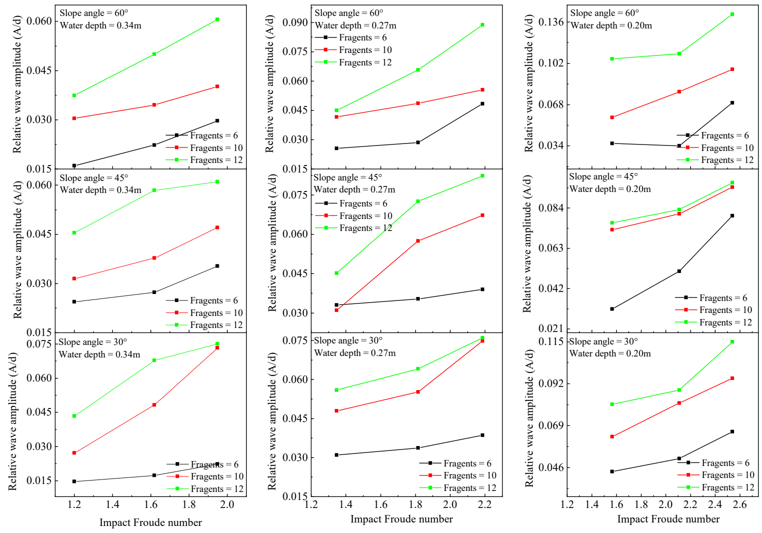

Fig. 8: Relationship between impact Froude number and relative wave ~~height~~amplitude.

3.1.3 Wave amplitude results

The results for the wave amplitude for various parameters are shown in Figs. 9, 10,

Formatted: Header

Formatted: Font: (Default) Times New Roman, Font color: Red

Formatted

Formatted: Normal, Centered, Don't adjust right indent when grid is defined, Space Before: 0 pt, Line spacing: 1.5 lines, No bullets or numbering, Don't adjust space between Latin and Asian text, Don't adjust space between Asian text and numbers, Tab stops: Not at 7.99 ch

Formatted

Formatted

and 11. As mentioned earlier, two gauges were used to measure the induced wave amplitude. Fig. 9 provides a detailed comparison of the wave amplitude recorded at both gauges for a 60° runup slope angle and a 0.445m445 m fall height. It can be observed that gauge-1, which is near to impact zone, has a higher relative amplitude compared to gauge-2. Furthermore, the results for the relative wave amplitude against the normalized time were also analyzedanalysed for all the water depths (0.20m20 m, 0.27m27 m, and 0.34m), 34 m), fall height (0.245m245 m, 0.445m445 m, and 0.645m645 m), and cliff height (0.12m12 m, 0.20m20 m, and 0.24m). 24 m). The results indicate that the wave amplitude increases as the cliff height, impact velocity, and number of fragments increase for all the water depths, as can be observed in Fig. 10, thus demonstrating that the potential energy of the falling cliff plays a critical role in the magnitude of the resulting wave.

Interestingly, comparing the wave amplitude induced by cliffs of various heights falling from the same height revealed that the water depth and the wave have an inverse relationship. As shown in Fig. 10 (a, b, and c), the average wave amplitude for various cliff heights and the same fall height of 0.245 m at 0.~~20m~~20 m water depth is 26% more than the average wave amplitude induced by 0.~~27m~~27 m water depth and 50% more than the 0.34m water depth wave amplitude. Similarly, Fig. 10 (d, e, and f) indicates that the average wave amplitude for 0.~~445m~~445 m fall height at 0.~~20m~~20 m water depth is 18% more than 0.027 m and 47% more than 0.34 m water depth, whereas, for 0.~~645m~~645 m fall height wave amplitude induced by 0.20 m water depth is 25% more than 0.~~27m~~27 m and 37% more than 0.~~34m~~34 m water depth (Fig. 10 g, h & i), thus suggesting that the deeper water dissipates the impact energy more effectively, as the deep water have more mass available to absorb and redistribute the impact energy, compared to shallower water thus reducing the overall amplitude of the induced wave. Moreover, a similar trend was observed for the wave amplitude involving 45°and 60°runup slope angle.

Later on, we performed another experiment by using granular material of equivalent mass as of cliff and slid it on a 30° slope, for all the water depths, and amplitude of the induced wave was measured as shown in Fig. 11. Fig. 11(a) indicates that the wave amplitude for 0.20 m water depth and 1.~~445kg~~445 kg granular mass (equivalent to 0.12 m cliff height) was 15% more than 0.~~27m~~27 m water depth and 65% more than wave amplitude induced by 0.34 m water depth. Whereas for 2.29kg and 2.82kg granular mass equivalent to 0.20 m and 0.24 m cliff height similar trend was observed as shown in Fig. 11 (b and c), thus indicating that as the water depth increases, the wave amplitude decreases for all the equivalent granular masses, as happened in the case of cliff fall.

Furthermore, a comparison between the wave amplitude induced by a falling cliff and equivalent granular mass at various water depths indicates that the amplitude of the wave induced by an equivalent granular mass in 0.~~34m~~34 m, 0.~~27m~~27 m, and 0.~~20m~~20 m water depth was on average 28%, 35% and 42% less than the wave amplitude induced falling cliff. The substantial difference in wave amplitude highlights the importance of energy transfer in wave formation. The falling cliff following a rotational motion imparts a more sudden and concentrated impact that allows an efficient energy transfer to water, leading to higher wave amplitudes. On the other hand, granular flows, being more deformable and flowing along a slope, result in gradual energy transfer over a wide area, thus resulting in lower wave amplitudes. The results highlight that it's not only the total impact energy that affects the behavior of the induced wave, but the mode of energy transfer also plays a critical role (Mohammed and Fritz, 2012; Wunnemann and Weiss, 2015). Based on the experimental results for wave amplitude and runup induced by rotational cliff collapse that fragments upon impact with the water surface, a novel prediction model was prepared using multi-expression programming. The justifications for the use of MEP have been well explained in the previous sections.

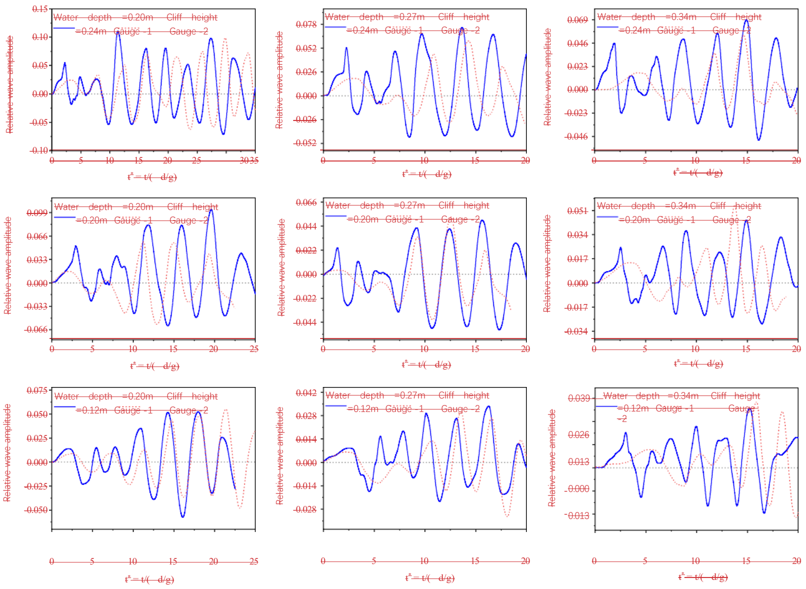

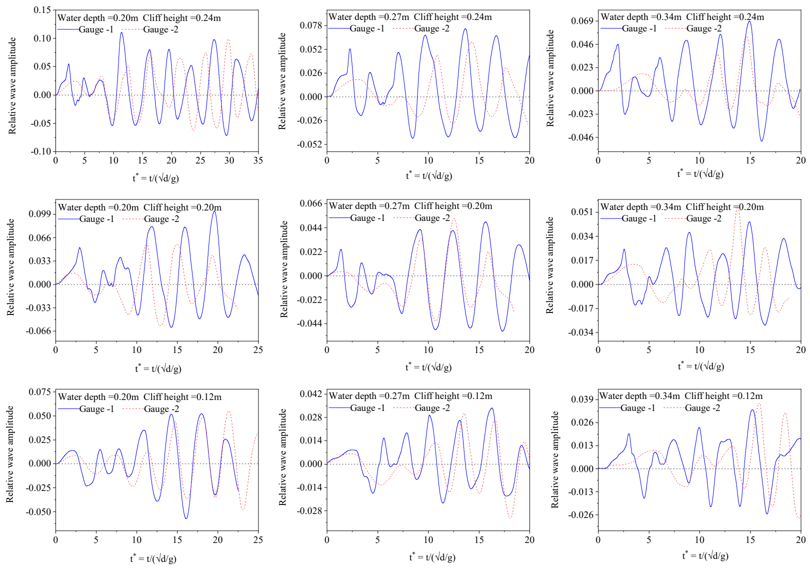

Fig. 9: A comparative display of the ~~wave~~water waves recorded at gauge 1&2 for a 60° slope angle, and 0.445 m fall height.

Formatted: Header

Formatted: Not Expanded by / Condensed by

Formatted: Not Expanded by / Condensed by

Formatted: Not Expanded by / Condensed by

Formatted: Not Expanded by / Condensed by

Formatted: Not Expanded by / Condensed by

Formatted: Font color: Red

Formatted: Font color: Red, Not Expanded by / Condensed by

Formatted: Font color: Red, Not Expanded by / Condensed by

Formatted: Not Expanded by / Condensed by

Formatted: Not Expanded by / Condensed by

Formatted: Not Expanded by / Condensed by

Formatted: Not Expanded by / Condensed by

Formatted: Not Expanded by / Condensed by

Formatted: Font: (Default) Times New Roman, 小四, Ligatures: None

Formatted: Font: (Default) Times New Roman, 小四, Not Expanded by / Condensed by , Ligatures: None

Formatted: Font: (Default) Times New Roman, 小四, Ligatures: None

Formatted: Font: (Default) Times New Roman, 小四, Not Expanded by / Condensed by , Ligatures: None

Formatted: Font: (Default) Times New Roman, 小四, Ligatures: None

Formatted: Font: (Default) Times New Roman, 小四, Not Expanded by / Condensed by , Ligatures: None

Formatted: Font: (Default) Times New Roman, 小四, Ligatures: None

Formatted: Font: (Default) Times New Roman, 小四, Not Expanded by / Condensed by , Ligatures: None

Formatted: Font: (Default) Times New Roman, 小四, Ligatures: None

Formatted: Font: (Default) Times New Roman, 小四, Not Expanded by / Condensed by , Ligatures: None

Formatted: Normal, Centered, Indent: Left: 0 cm, Don't adjust right indent when grid is defined, Line spacing: single, Don't adjust space between Latin and Asian text, Don't adjust space between Asian text and numbers, Tab stops: Not at 18.67 ch

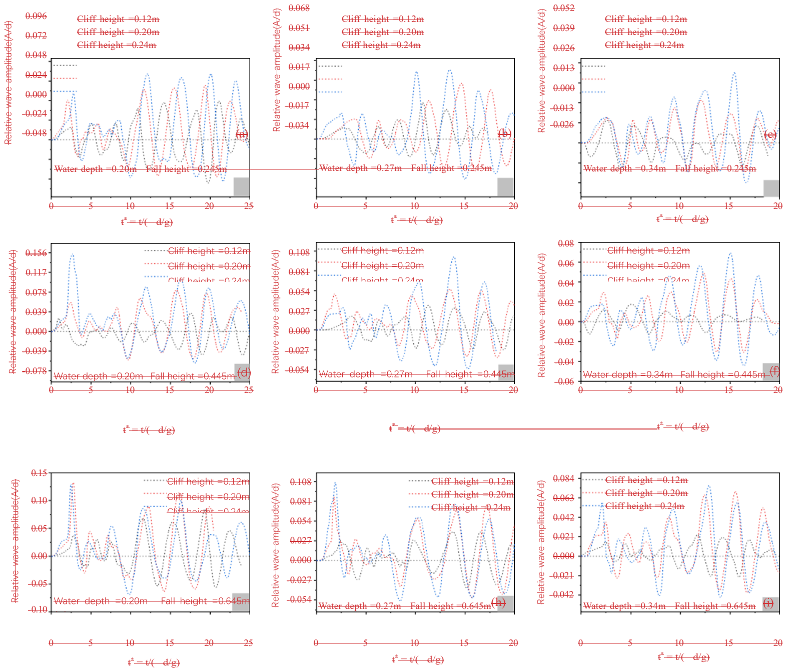

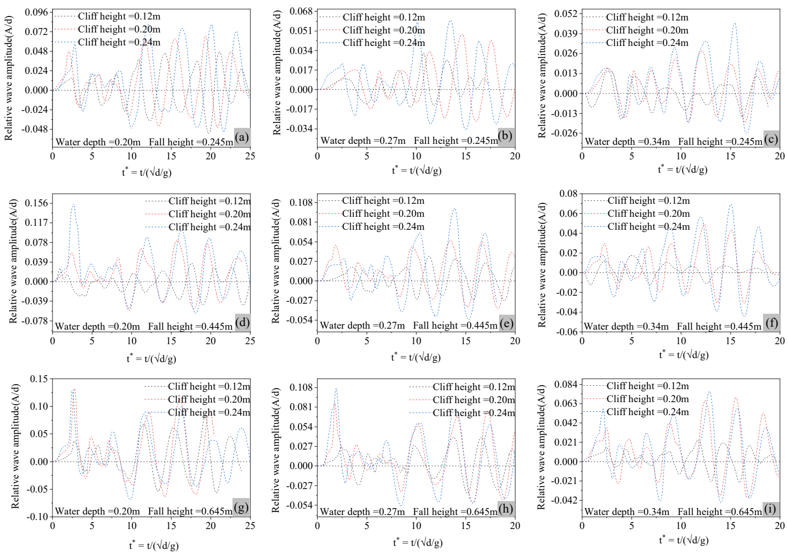

Fig. 10: Relative wave amplitude for various water depths, cliff height, and fall height at 30°runup slope angle, (a, b&c) relative wave amplitude induced by 0.245 m fall

height, (d, e&f) relative wave amplitude induced by 0.445m445 m fall height, (g, h&i) relative wave amplitude induced by 0.645m645 m fall height.

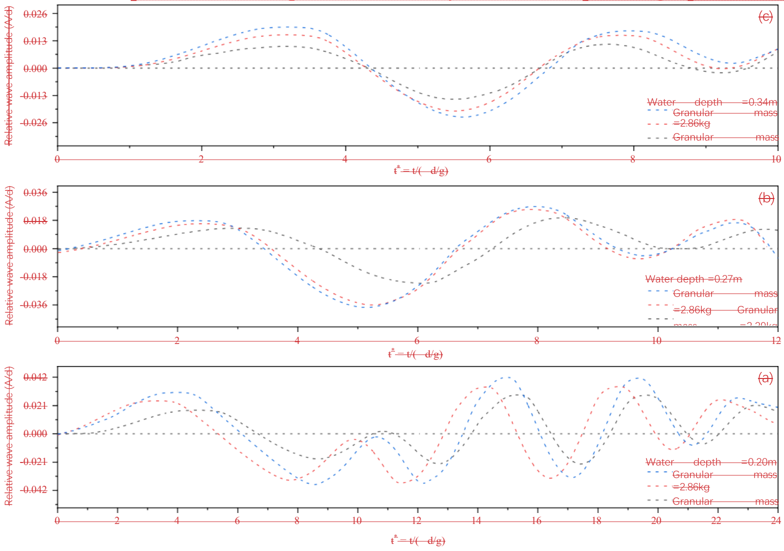

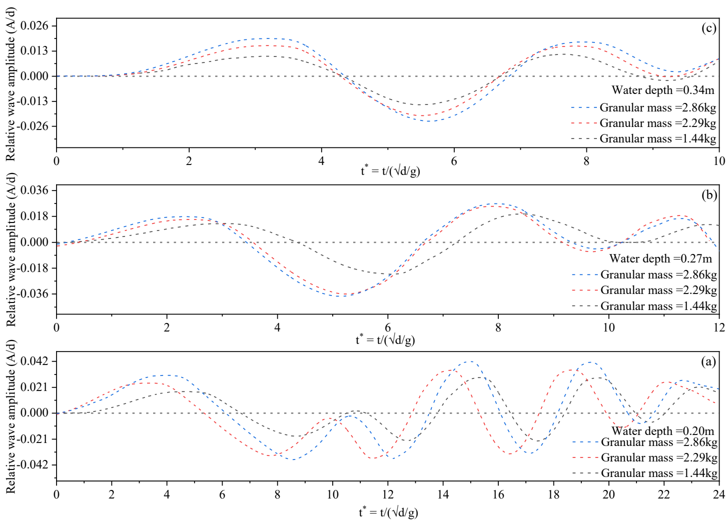

Fig. 11: WaveWater waves induced by equivalent granular mass at 30° slope angle

Formatted: Header
Formatted: Font color: Red
Formatted: Font color: Red, Not Expanded by / Condensed by
Formatted: Font color: Red
Formatted: Font color: Red, Not Expanded by / Condensed by
Formatted: Font color: Red
Formatted: Font color: Red, Not Expanded by / Condensed by
Formatted: Font color: Red
Formatted: Font color: Red, Not Expanded by / Condensed by
Formatted: Font color: Red
Formatted: Font color: Red, Not Expanded by / Condensed by
Formatted: Font color: Red
Formatted: Font color: Red, Not Expanded by / Condensed by
Formatted: Font color: Red
Formatted: Font color: Red, Not Expanded by / Condensed by
Formatted: Font color: Red
Formatted: Font color: Red, Not Expanded by / Condensed by
Formatted: Font color: Red
Formatted: Font color: Red, Not Expanded by / Condensed by
Formatted: Font color: Red
Formatted: Font color: Red, Not Expanded by / Condensed by
Formatted: Font: (Default) Times New Roman, (Asian) +Body Asian (等线), 小四, Font color: Red, Ligatures: None
Formatted: Font: (Default) Times New Roman, (Asian) +Body Asian (等线), 小四, Font color: Red, Not Expanded by / Condensed by , Ligatures: None
Formatted: Font: (Default) Times New Roman, (Asian) +Body Asian (等线), Font color: Red
Formatted: Normal, Centered, Indent: Left: 0 cm, Don't adjust right indent when grid is defined, Line spacing: single, Don't adjust space between Latin and Asian text, Don't adjust space between Asian text and numbers, Tab stops: Not at 13 ch
Formatted: Font: (Default) Times New Roman, (Asian) +Body Asian (等线), 小四, Font color: Red, Ligatures: None
Formatted: Font: (Default) Times New Roman, (Asian) +Body Asian (等线), 小四, Font color: Red, Not Expanded by / Condensed by , Ligatures: None
Formatted ...
Formatted ...

3.2 Numerical modeling results

The numerical simulations conducted in this study successfully captured key dynamic characteristics of the wave generated by the rotational cliff collapse, specifically the wave amplitude and wave runup, across a range of test cases. Moreover, the front velocity of the incident wave was also measured. The simulations were also focused on verifying the results obtained from the rotational cliff collapse in the experiments. To quantify the wave amplitude, runup, and velocity, a post-processing technique was employed. To establish the reliability of the wave front velocity measurements, the velocity was calculated at 5–7 distinct locations along the wave's propagation path and at multiple time steps during the simulation. This multi-point sampling approach minimized errors due to spatial and temporal variations. Fig. 12 shows a representative case of wave formation and propagation in a water tank at a depth of d = 0.2 m at various time frames.

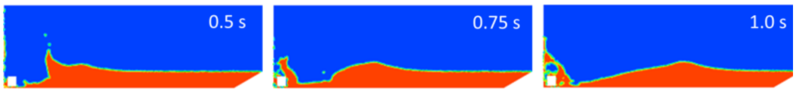

~~Fig. 12 Wave formation and propagation at water depth of d = 0.2 m at various time frames.~~

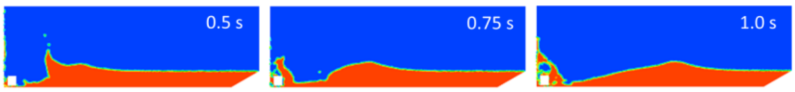

Fig. 12: Wave formation and propagation at water depth of d = 0.2 m at various time frames.

The wave amplitude was defined as the peak vertical displacement of the liquid surface relative to the undisturbed free surface level. Fig. 13 illustrates a representative case, depicting the wave front propagation.

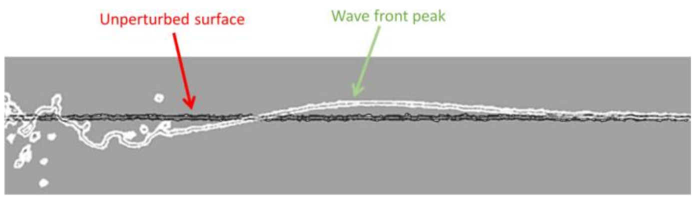

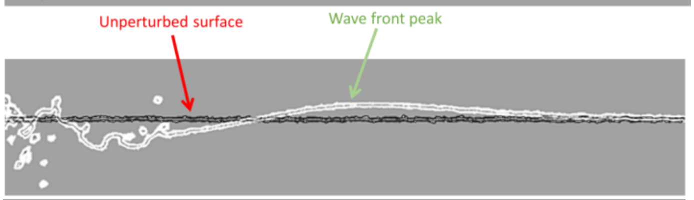

Fig. 13: Wave dynamics following a rotational cliff collapse in water depth d = 0.34

m. Stable liquid surface before impact (black line); wave front propagating ~~to~~away from the ~~right~~point of impact (white line).

To validate the results of simulations, we compared the results of the runup height with the experimental values. Table 3 presents the runup values for various

Formatted: Header

Formatted ...

Formatted: Normal, Centered, Indent: Left: 0 cm, First line: 0 cm, Right: 0 cm, Space Before: 0 pt, Line spacing: 1.5 lines

Formatted ...

runup slope angles, i.e., 30°, 45°, and 60°, for a water depth of ~~d=~~0.~~27m~~27 m. The comparison of simulated values was performed at this depth, as it lies in the middle of the experimental test range of water depths. Numerical modeling results indicate that for a fixed water depth, the runup values consistently decrease as the runup slope angle increases from 30° to 60°. At a water depth of ~~d=~~0.27 m, the runup decreases from 0.2 m at 30° to 0.17 m at 45°, and further to 0.11 m at 60°. This reduction is attributed to the changing momentum transfer dynamics with increasing slope angle. At less steep angles (closer to horizontal, e.g., 30°), the rock's momentum generates a stronger radial splash and greater upslope displacement of the liquid along the cliff. As the angle increases toward 60°, a larger component of the momentum is directed parallel to the cliff, reducing the vertical impulse. The experimental and numerical results agree well, and the difference lies within the acceptable range of 4-5%. The experimental results for the other two water depths also indicate similar behavior.

Table 3: Peak runup values along the various slope angles at a water depth of ~~d=~~0.~~27m~~27 m

Depth *d* (m)	**Numerical-30°**	**Exp-30°**	**Numerical-45°**	**Exp-45°**	**Numerical-60°**	**Exp-60°**
0.27	0.20	0.19	0.17	0.16	0.11	0.102

Next, we measured the wave velocity through the numerical results, as it wasn't captured accurately through experimental images. Fig. 14 illustrates the simulated wave fronts at a time instant of t =1 second following the impact of the solid rock on the liquid pool, for various water depths and a fixed slope angle of 30 degrees. These visualizations highlight the propagation of the waves from the impact zone. The slope angle was varied across simulations to assess its influence on wave characteristics. It was observed that changes in the slope angle induced only minor variations in both the wave front velocity and wave amplitude for a given pool depth. These perturbations were typically within 1–2% of the mean values. Consequently, to streamline the analysis and focus on dominant trends, the wave front velocity and height were averaged over the range of slope angles for each specific water depth.

However, variations in water depth exerted a pronounced effect on the wave

Formatted: Header

Formatted

Formatted: Normal, Left, Indent: Left: 0 cm, First line: 0.74 cm, Right: 0 cm, Space Before: 0 pt, Line spacing: 1.5 lines

Formatted

Formatted

Formatted: Font: 10 pt, Font color: Text 1, Not Expanded by / Condensed by

Formatted: Font: 10 pt, Font color: Text 1, Not Expanded by / Condensed by

Formatted: Font: 10 pt, Font color: Text 1, Not Expanded by / Condensed by

Formatted: Font: 10 pt, Font color: Text 1, Not Expanded by / Condensed by

Formatted: Font: 10 pt, Font color: Text 1, Not Expanded by / Condensed by

Formatted: Font: 10 pt, Font color: Text 1, Not Expanded by / Condensed by

Formatted

Formatted

Formatted: Font: 10 pt, Font color: Text 1, Superscript

Formatted

Formatted: Font: 10 pt, Font color: Text 1

Formatted

Formatted: Font: 10 pt, Font color: Text 1, Superscript

Formatted

Formatted

Formatted

Formatted: Font: 10 pt, Font color: Text 1

Formatted

Formatted

Formatted: Font: 10 pt, Font color: Text 1, Superscript

Formatted

Formatted: Font: 10 pt, Font color: Text 1

Formatted

Formatted

Formatted

Formatted

Formatted

Formatted: Font: 10 pt, Font color: Text 1

Formatted

Formatted

Formatted

Formatted

Formatted

Formatted

Formatted

Formatted

Formatted

Formatted

Formatted

dynamics, leading to significant alterations in both the propagation velocity and amplitude of the generated waves. This depth-dependent behavior is quantified in Table 4, which presents the averaged results from the numerical simulations. For a shallow water depth of d=0.2 m, the average wave front velocity was computed as 1.48 m/s, with a corresponding average wave height of 0.11 m. As the pool depth increased to d=0.27 m, the velocity rose to 1.58 m/s, while the wave height decreased to 0.07 m. Further deepening to d=0.34 m yielded a velocity of 1.74 m/s and a reduced wave heightamplitude of 0.06 m. These trends indicate an approximately linear increase in velocity with depth, accompanied by an inverse relationship for wave amplitude.

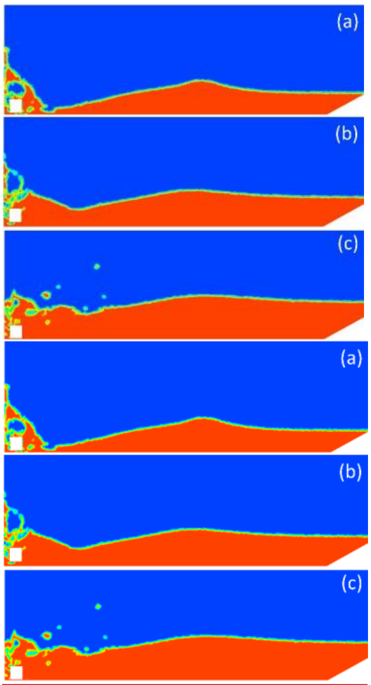

Fig. 14: Propagating wave fronts after the impact at time t = 1 s for a slope angle of 30-degree. (a) d = 0.2 m, (b) d = 0.27 m, (c) d = 0.34 m.

The observed depth dependence can be rationalized through fundamental principles of wave propagation in gravity-dominated, multi-phase flows. In the shallow water regime, given that the pool depths (0.2–0.34 m) are comparable to or smaller than the wavelengths of the generated waves, the phase velocity c of long gravity waves approximates c≈$gh, $c\approx\sqrt{gh}$, where g is the gravitational acceleration (9.81 m/s²)²), and h is the undisturbed water depth. This relation arises from the shallow water equations, where hydrostatic pressure balance and negligible vertical acceleration dominate, leading to a dispersionless incident wave speed that scales with the square root of depth. Substituting the water depths yields theoretical velocities of approximately 1.40 m/s for *d*=0.2 m, 1.63 m/s for *d*=0.27 m, and 1.83 m/s for *d*=0.34 m, which align closely with the simulated values (discrepancies of 7–10% may stem from viscous dissipation, non-

Formatted: Header

Formatted

Formatted

Formatted

Formatted

hydrostatic effects near the impact zone, or spreading of the wave front). A comparative analysis of the results is shown in Table 4.

Conversely, the decrease in wave amplitude with increasing water depth aligns with energy conservation and volume displacement considerations in impact-generated waves. The impact of rotational cliff collapse imparts a fixed kinetic energy and displaces a finite volume of liquid, creating an initial cavity and subsequent outflow that evolves into a propagating wave. In shallower pools, the displaced volume is confined to a smaller cross-sectional area, resulting in greater vertical amplification to accommodate the same mass redistribution. For deeper water depths, the energy is distributed over a larger water column, diluting the surface perturbation and yielding lower amplitudes. The trends observed in the numerical simulations for water waves induced by rotational cliff collapse are in good agreement with theoretical and experimental results, indicating that water depth has a direct effect on the wave velocity and an inverse effect on the wave amplitude and runup.

Table 4: The average wave propagation velocity and amplitude for various water depths.

Water depth *d* (m)	**Avg. wave velocity *v* (m/s)**	**Theoretical wave velocity *c* (m/s)**	**Wave amplitude *A* (m)**
0.2	1.48	1.40	0.11
0.27	1.58	1.63	0.07
0.34	1.74	1.83	0.06

~~3.3 MEP model results~~

~~The purpose was to develop a precise model for wave amplitude and runup induced by rotational cliff collapse. The predicted model is a function of seven variables, i.e., water depth, fall height, cliff mass, impact velocity, cliff height, runup slope angle, and number of fragments, and can be described as follows,~~

$$\text{Wave amplitude and runup} = f(d, H, m, v, h, \alpha, N_f) \quad (3)$$

~~The relation among the parameters was evaluated using Pearson's correlation to analyze the multicollinearity and interdependency between the parameters, as they can~~

3.3 MEP model results

The purpose was to develop a precise model for wave amplitude and runup induced by rotational cliff collapse. The predicted model is a function of seven variables, i.e., water depth, fall height, cliff mass, impact velocity, cliff height, runup slope angle, and number of fragments, and can be described as follows,

$$Wave\ amplitude\ and\ runup\ = f\left(d, H, m, v, h, \alpha, N_f\right) \quad (3)$$

The relation among the parameters was evaluated using Pearson's correlation to analyze the multicollinearity and interdependency between the parameters, as they can obscure the interpretation of the developed model. The model was developed by splitting the data into two subsets, i.e., training (70%) and testing (30%). The randomization was done by MEP itself. Following the criteria, 70% of the data, i.e., 57 data points, were taken as training data, whereas 30% of the data, i.e., 24 data points, were considered for validation of the model. The mathematical expression for MEP is obtained by solving the C++ code and representing it as per optimized hyperparameter settings, as shown in Table 5. The prediction model for wave amplitude and runup was developed by analyzing the MEP code in MATLAB, as shown in Equations 4 and 5.

Table 5: Parametric settings of the MEP algorithm for wave amplitude and runup

Sr.No.	Parameters	Wave amplitude	Wave runup
1	Number of sub-populations	125	85
2	Sub-population size	115	75
3	Crossover probability	0.85	0.60
4	Code length	35	25
5	Tournament size	30	10
6	Mutation probability	0.085	0.06
7	Number of generations	250	120
8	Crossover type	Uniform	Uniform
9	Error measure	Mean absolute error	Mean absolute error
10	Problem type	Regression	Regression
11	Function set	+, -, x, /, ^	+, -, x, /, ^
12	Terminal set	Problem Input	Problem Input
13	Operators	0.5	0.5
14	Simplified	Yes	Yes
15	Variables	0.5	0.5
16	Random seed	0	0
17	Constants	0	0

$$Wave\ amplitude\ A = d^{\left(\frac{\alpha}{d(dGN_fGm)}\right)} + \frac{2vh^K}{m+N_f+d(d+N_f+m)} + 2vhd^{\left(\frac{\alpha}{d(dGN_fGm)}\right)} \quad (4)$$

$$Wave\ runup\ R = \frac{A\left(h+\left(A\cdot\left(d-\frac{B}{\alpha}\right)\right)\right)^{B/\alpha-M}\cdot B}{\alpha} \quad (5)$$

$$A = v + h^d$$

$$B = v + m + h^d$$

$$Wave\ amplitude\ A = d^{\left(\frac{\alpha}{d(d+N_f+m)}\right)} + \frac{2vh^2}{m+N_f+d(d+N_f+m)} + 2vhd^{\left(\frac{\alpha}{d(d+N_f+m)}\right)} \quad (4)$$

$$Wave\ runup\ R = \frac{A\left(h+\left(A\cdot\left(d-\frac{B}{\alpha}\right)\right)^{B/\alpha}\right)^{A}\cdot B}{\alpha} \quad (5)$$

$$A = v + h^d$$

$$B = v + m + h^d$$

Whereas d is the water depth (m), m is the mass of the cliff (kg), v is the impact velocity (m/s), h is the cliff height (m), α is the runup slope angle, and N_f is the number of fragments.

3.3.1 Prediction performance of the developed model

The robustness of the proposed model was evaluated by comparing it with well-established statistical indices, i.e., mean absolute error (MAE), root mean square error (RMSE), correlation coefficient (Cr), Nash–Sutcliffe efficiency (NSE), and performance index (PI). The indices can be represented by equation (6-10) (Khan et al., 2022).

established statistical indices, i.e., mean absolute error (MAE), root mean square error (RMSE), correlation coefficient (Cr), Nash Sutcliffe efficiency (NSE), and performance index (PI). The indices can be represented by equation (6-10) (Alavi et al., 2010; Khan et al., 2022).

$$MAE = \frac{\sum_{i=1}^{n} |e_i - p_i|}{n} \quad (6)$$

$$RMSE = \frac{\sum_{i=1}^{n} (e_i - p_i)^2}{n} \quad (7)$$

$$NSE = 1 - \frac{\sum_{i=1}^{n} (e_i - p_i)^2}{\sum_{i=1}^{n} (e_i - \bar{e}_i)^2} \quad (8)$$

$$PI = \frac{RRMSE}{1+R} \quad (9)$$

$$R^2 = \left(\frac{\sum_{i=1}^{n} (e_i - \bar{e}_i)(p_i - \bar{p}_i)}{\sum_{i=1}^{n} (e_i - e_i)^2 \sum_{i=1}^{n} (P_i - \bar{P}_i)^2} \right)^2 \quad (10)$$

Whereas, $\bar{e}_i$ and $\bar{p}_i$ are the average values of the experimental and predicted results, and e_i and p_i are i_{th} values of the modeled and predicted results, for n total samples. It is good to consider the error indices while analyzing the predictive capability of complex models. The wave runup model demonstrated a robust performance for both training and testing datasets. The lower values of RMSE and MAE indicate little deviation from experimental values, while RSE and RMSE values confirm lower normalized error, as shown in Table 6. The higher values of NSE and Cr further validated the model reliability for the training phase. Whereas for the validation dataset, i.e., the unseen data model displays even stronger performance with lower RMSE and MAE values compared to the training dataset. Moreover, higher Cr and lower performance index values highlight enhanced model efficiency. This suggests that the model works well for unseen data, making it suitable for predicting the wave runup induced by rotational cliff collapse (Gardezi et al., 2024).).

The predictive performance of the wave amplitude model in the case of training data demonstrated a strong correlation with high R^2 values and low RMSE and MAE

Formatted: Header

Formatted

Formatted

Formatted

Formatted

Formatted

Formatted

Formatted

Formatted

Formatted

Formatted

Formatted

Formatted: Normal, Indent: First line: 0.74 cm, Don't adjust right indent when grid is defined, Space Before: 0 pt, Line spacing: 1.5 lines, No bullets or numbering, Don't adjust space between Latin and Asian text, Don't adjust space between Asian text and numbers, Tab stops: Not at 5.87 ch

Formatted

Formatted

values corresponding to 13.14% relative error, thus suggesting a good agreement between experimental and predicted values, as shown in Table 6. The higher NSE and C_r values further confirmed the model's reliability for the training dataset with minimal systematic bias. When the model was exposed to unseen data, it still maintained reasonable accuracy with an R^2 value of 0.78. Though the values of error matrices, i.e., RMSE, MAE, and RRMSE, are a bit higher than the training data set, this is expected due to inherent generalization challenges. Similarly, the higher NSE and C_r values, though lower than the training dataset, indicate consistent predictive performance of the wave amplitude model with little increase in bias. Overall model exhibited strong predictive performance in the training and testing phase, with a little expected decline in the validation phase.

Table 6: Performance index values for the MEP-based velocity prediction model.

water Performance parameters	Wave Amplitude		Wave Runup	
	Training data	Validation data	Training data	Validation data
RSQ	0.8823	0.7811	0.8748	0.9691
RMSE	0.00178	0.0025	0.01327	0.00617
MAE	0.00135	0.00176	0.0108	0.00504
RSE	0.1180	0.2439	0.1306	0.0312
RRMSE	0.1314	0.1594	0.1472	0.0660
P. index	0.0698	0.0908	0.076	0.0333
NSE	0.8819	0.7560	0.8693	0.9687
C_r	0.9393	0.8829	0.9353	0.9844

Previously, scientists have also used the slope of the regression line as a performance indicator for AI models, thus representing a correlation between experimental and predicted results. Fig. 15 (a & b) shows the regression line for our wave amplitude and runup model. For wave amplitude, the slope value for the trainingprediction model. data set is 0.88, which is adequate, and 0.78 in validation, which is still greater than the minimum value of 0.7; it can happen as the model involving numerous parameters and complex phenomena usually performs slower for the unseen data(Yarkoni and Westfall, 2019). Whereas, for wave runup, the model performed very well for both training and validation data sets with an R^2 value of 0.87 and 0.96, respectively.

The accuracy of the proposed model can also be checked using residual error plots, which are obtained by subtracting experimental and predicted values (Alavi et al., 2013). The results indicate that the amplitude model has minimum and maximum values of 0.004 m and 0.0065 m, as shown in Fig. 16 (a), whereas for wave runup the minimum and maximum values are -0.01875 and 0.024 (Fig. 16b). Moreover, it can also be observed that error values are populated along the x-axis, therefore, showing low error frequency, and accuracy of both the models.

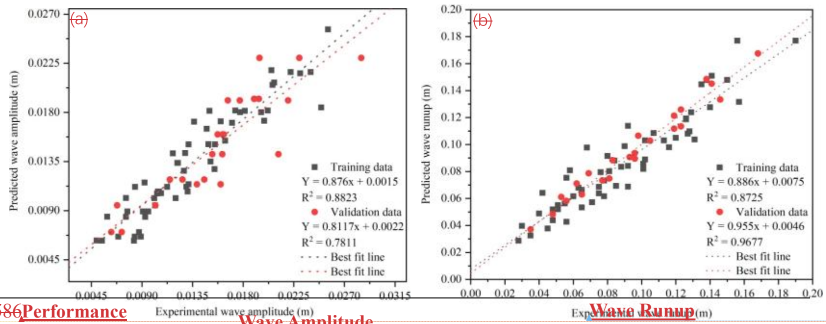

Fig. 15 Tracing the experimental results by predicted values, (a) wave amplitude and (b) wave runup

Performance parameters	Wave Amplitude		Wave Runup	
	Training data	Validation data	Training data	Validation data
RSQ	0.8823	0.7811	0.8748	0.9691
RMSE	0.00178	0.0025	0.01327	0.00617
MAE	0.00135	0.00176	0.0108	0.00504
RSE	0.1180	0.2439	0.1306	0.0312
RRMSE	0.1314	0.1594	0.1472	0.0660
P. index	0.0698	0.0908	0.076	0.0333
NSE	0.8819	0.7560	0.8693	0.9687
C_r	0.9393	0.8829	0.9353	0.9844

Previously, scientists have also used the slope of the regression line as a performance indicator for AI models, thus representing a correlation between experimental and predicted results. Fig. 15 (a & b) shows the regression line for our wave amplitude and runup model. For wave amplitude, the slope value for the training data set is 0.88, which is adequate, and 0.78 in validation, which is still greater than the minimum value of 0.7; it can happen

Formatted: Header
Formatted
Inserted Cells
Merged Cells
Formatted
Formatted: Normal, Centered, Indent: Left: 0 cm, Line spacing: single
Formatted: Font: (Asian) +Body Asian (等线), Not Expanded by / Condensed by
Formatted: Font: Bold
Formatted: Normal, Centered
Inserted Cells
Formatted: Normal, Centered, Indent: Left: 0 cm, Space Before: 0 pt
Formatted: Font: Times New Roman, 10 pt, Bold
Formatted: Normal, Centered, Indent: Left: 0 cm, Space Before: 0 pt, Line spacing: single
Inserted Cells
Formatted
Inserted Cells
Inserted Cells
Formatted: Font: Times New Roman, 10 pt
Formatted: Normal, Centered, Indent: Left: 0 cm, Line spacing: single
Formatted Table
Inserted Cells
Formatted: Font: 10 pt
Formatted: Normal, Centered, Indent: Left: 0 cm, Space Before: 0 pt, Line spacing: single
Formatted

as the model involving numerous parameters and complex phenomena usually performs slower for the unseen data (Yarkoni and Westfall, 2019). Whereas, for wave runup, the model performed very well for both training and validation data sets with an R^2 value of 0.87 and 0.96, respectively.

The accuracy of the proposed model can also be checked using residual error plots, which are obtained by subtracting experimental and predicted values. The results indicate that the amplitude model has minimum and maximum values of -0.004 m and 0.0065 m, as shown in Fig. 16 (a), whereas for wave runup the minimum and maximum values are -0.01875 and 0.024 (Fig. 16b).

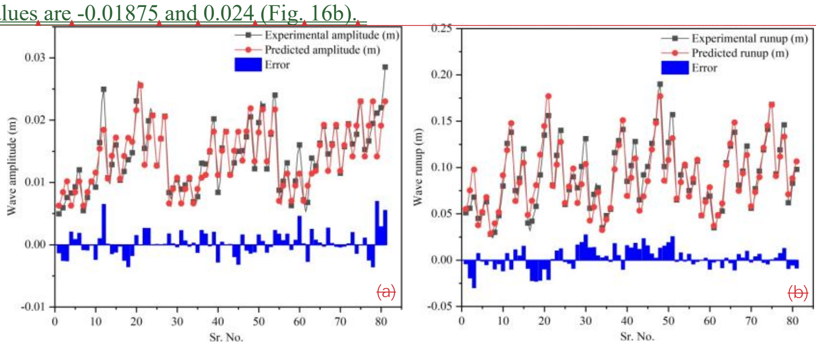

Fig. 16 Indicating error values between experimental and predicted model (a) wave amplitude, and (b) Wave runup

3.2 Validation of the developed model

The validation of the proposed model is an important feature in predictive modeling. It has been observed that sometimes the model performs very well for training data sets,

Formatted: Header

Formatted: Not Expanded by / Condensed by

Formatted: Not Expanded by / Condensed by

Formatted: Not Expanded by / Condensed by

Formatted: Not Expanded by / Condensed by

Formatted: Not Expanded by / Condensed by

Formatted: Not Expanded by / Condensed by

Formatted: Not Expanded by / Condensed by

Formatted: Not Expanded by / Condensed by

Formatted: Not Expanded by / Condensed by

Moreover, it can also be observed that error values are populated along the x-axis, therefore, showing low error frequency, and accuracy of both the models.

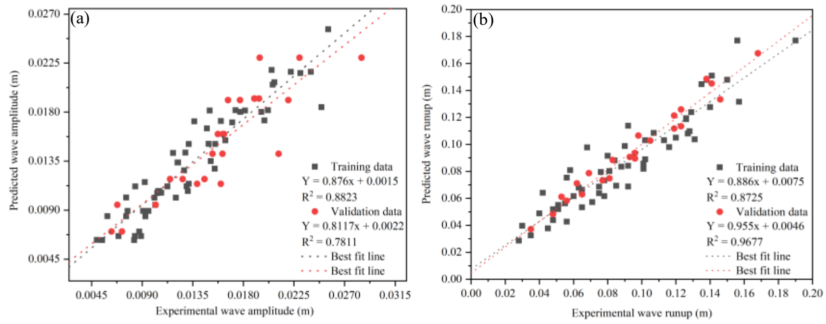

Fig. 15 Tracing the experimental results by predicted values, (a) wave amplitude and (b) wave runup

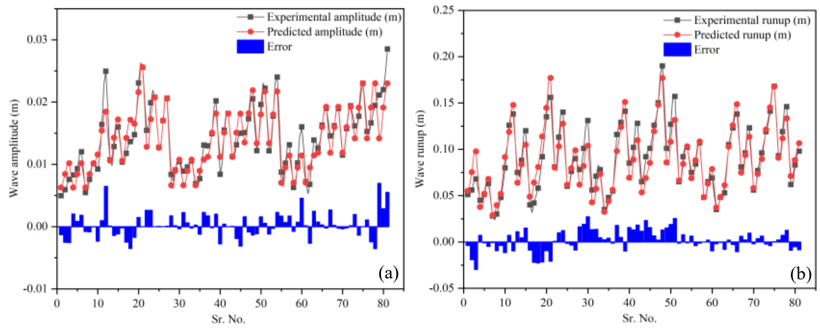

Fig. 16 Indicating error values between experimental and predicted model (a) wave amplitude, and (b) Wave runup

3.2 Validation of the developed model

The validation of the proposed model is an important feature in predictive modeling. It has been observed that sometimes the model performs very well for training data sets, but fails to perform during the validation stage for unseen data. So, the developed prediction model was further validated by conducting the sensitivity and parametric analysis for both the wave amplitude and runup.

3.2.1 Sensitivity analysis

Sensitivity and parametric analysis play a vital role in determining the robustness of the proposed model. The sensitivity analysis (SA) of the developed prediction model for the entire dataset tells us how sensitive the model is to any changes in input parameters. So, for an independent parameter Y_i the SA can be calculated using equations 11 and 12, which indicates that for any parameter, the values were varied between two extremes, and others were constant at their average, and the outcome was found in the form of Y_i, and then the same process was repeated for all the remaining parameters.

$$R_k = f_{max}(Y_k) - f_{min}(Y_k) \quad (11)$$

Formatted: Header

Formatted: Normal, Left, Indent: Left: 0 cm, First line: 0.74 cm, Right: 0 cm, Don't adjust right indent when grid is defined, Space Before: 0 pt, Line spacing: 1.5 lines, Don't adjust space between Latin and Asian text, Don't adjust space between Asian text and numbers

Formatted: Font: (Default) Times New Roman, 小四

Formatted

Formatted

$$R_k = f_{max}(Y_k) - f_{min}(Y_k) \quad (11)$$

Relative Importance

$$SA\,(\%) = \frac{R_k}{\sum_{j=1}^{n} R_j} \times 100 \quad (12)$$

Whereas, $f_{max}(Y_k)$ and $f_{min}(Y_k)$ represent the minimum and maximum values of the model-based results grounded on the *kth* domain of the input parameters in the above equation. Fig. 17 (a & b) shows the results of the sensitivity analysis of the developed prediction model for the wave amplitude and runup. Figure 17 (a) indicates that the wave amplitude is greatly influenced by the height of the cliff (h) and has an effect of almost 51%. The water depth (d) contributes 4.36% to wave amplitude, cliff mass (m) contributes 4.69%, and impact velocity (v) and number of fragments (N_f) contribute 18% and 22% to the induced wave amplitude. Whereas the fall height (H) and runup slope angle (α) do not affect the wave amplitude. Since the impact velocity parameters have already catered for the fall height that's why it is not visible in the proposed model. The model tells us that impact velocity, cliff height, and number of fragments contribute approximately 90% to the wave amplitude induced by the rotational fall of the cliff. It can be concluded that the effect of $h > N_f > v > m > d$ on the induced wave amplitude.

Similarly, the sensitivity analysis of wave runup (Fig. 17b) indicates that runup is greatly influenced by bank slope angle (α) and has an effect of 34%. Impact velocity ~~(v~~ (v) contributes 25.3%, cliff mass ~~(m~~m) 20.3%, cliff height (h) 13.3%, and water depth ~~(d~~ (d) contributes around 7% to wave runup. Whereas, the number of fragments and fall height that have already been catered in impact velocity don't contribute to wave runup. This suggests that wave runup is primarily governed by coastal geometry, i.e., bank slope angle and cliff height, and hydrodynamic forces, i.e., impact velocity, whereas water depth contributes a little to wave runup. It can also be concluded as the effect of $\alpha > v > m > h > d$ on the induced wave amplitude.

~~$\alpha > v > m > h > d$ on~~

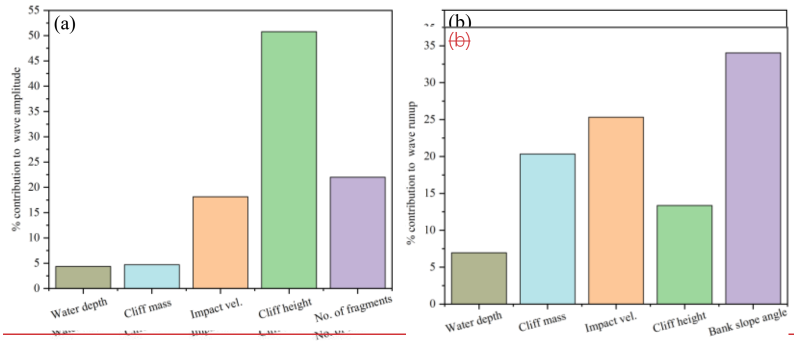

Fig. 17 Sensitivity analysis of the ~~induced~~MEP-based wave amplitude~~.~~ and runup prediction model

~~Fig. 17 Sensitivity analysis of the MEP-based wave amplitude and runup model~~

~~**3.2.2 Parametric Analysis**~~

~~Parametric analysis results for the input parameters for the wave amplitude used in this study are displayed in Fig. 18. The parametric analysis indicates that wave amplitude decreases as the water depth, number of fragments, and cliff mass increase, whereas it increases with the increase in cliff height and impact velocity. These trends~~

Formatted: Header

Formatted: Normal, Indent: First line: 0.74 cm, Don't adjust right indent when grid is defined, Line spacing: 1.5 lines, No bullets or numbering, Don't adjust space between Latin and Asian text, Don't adjust space between Asian text and numbers, Tab stops: Not at 5.87 ch

Formatted: Font: (Default) Times New Roman

Formatted: Normal, Centered, Indent: First line: 0.74 cm, Don't adjust right indent when grid is defined, Space Before: 0 pt, Line spacing: 1.5 lines, No bullets or numbering, Don't adjust space between Latin and Asian text, Don't adjust space between Asian text and numbers, Tab stops: Not at 5.87 ch

Formatted: Header

are in line with the fundamental physics principles (Bougouin et al., 2020; Lipiejko et al., 2023)—deep waters dissipate more energy, and greater impact velocities and larger cliff heights impart more kinetic and potential energies to water bodies for wave generation. Whereas, the inverse relation between the number of fragments and wave amplitude proposes a potential threshold effect in which initial fragmentation contributes to wave formation, whereas excessive fragments contribute to energy dissipation owing to increased turbulence. The sensitivity analysis further quantified the effect of these parameters, classifying cliff height as a major contributing factor in

3.2.2 Parametric Analysis

Parametric analysis results for the input parameters for the wave amplitude used in this study are displayed in Fig. 18. The parametric analysis indicates that wave amplitude decreases as the water depth, number of fragments, and cliff mass increase, whereas it increases with the increase in cliff height and impact velocity. These trends are in line with the fundamental physics principles (Bougouin et al., 2020; Lipiejko et al., 2023). Deep waters dissipate more energy, and greater impact velocities and larger cliff heights impart more kinetic and potential energies to water bodies for wave generation. In contrast, the inverse relation between the number of fragments and wave amplitude proposes a potential threshold effect in which initial fragmentation contributes to wave formation, whereas excessive fragments contribute to energy dissipation owing to increased turbulence. The sensitivity analysis further quantified the effect of these parameters, classifying cliff height as a major contributing factor in wave amplitude variations, followed by impact velocity, number of fragments, water depth, and mass of cliff. The strong influence of cliff height indicates its direct effect in determining the potential energy for wave generation. Moreover, the larger sensitivity value of fragments regardless of their inverse parametric relation shows a complex relation, where fragment count plays a considerable but context-dependent role in wave generation and propagation. The dominance of cliff height, impact velocity, and fragment count suggests that these parameters should be prioritized in future prediction models. These findings are important for developing predictive models for wave generations due to rotational cliff collapse.

The developed model for wave amplitude provides valuable insights into fundamental physics governing wave formation and propagation induced because of rotational cliff collapse. The strong height dependence of the model confirms the classical principle of conservation of potential energy, whereas the fragment count dependence reveals energy partitioning mechanisms. The results of performance indices and sensitivity, and parametric analysis increase our understanding of how geometric and dynamic characteristics govern the wave characteristics, with relevance to hazard assessment and disaster mitigation in coastal regions prone to cliff collapse following rotational motion.

The results of the parametric analysis for wave runup are presented in Fig. 19. It can be observed from Fig. 19 (a & e) that as the water depth and bank slope angle increase, the wave runup decreases, due to energy dissipation and different wave breaking dynamics. Conversely, as the cliff mass, cliff height, and impact velocity increase, the wave runup increases, as greater kinetic energy and inertia impart greater uprush. Notably, all the parameters present a strong correlation with the runup (more than 97%), highlighting their statistical significance. The results agree with the general physics laws, where mild slopes and larger impact forces result in higher runups, whereas deep waters attenuate wave energy.

An important observation from parametric analysis of wave amplitude and runup, as shown in Fig. 18b, and 19c, indicates that cliff mass represents a nonlinear relation with wave amplitude and a linear relation with runup. This is due to the fact that the

Formatted: Header

Formatted: Font: (Default) Times New Roman, 五号

Formatted: Font: (Default) Times New Roman, 五号, Not Expanded by / Condensed by

Formatted: Font: (Default) Times New Roman, 五号

Formatted: Font: (Default) Times New Roman, 五号, Not Expanded by / Condensed by

Formatted: Font: (Default) Times New Roman, 五号

Formatted: Font: (Default) Times New Roman, 五号, Not Expanded by / Condensed by

Formatted: Font: (Default) Times New Roman, 五号

Formatted: Font: (Default) Times New Roman, 五号, Not Expanded by / Condensed by

Formatted: Font: (Default) Times New Roman, 五号

Formatted: Font: (Default) Times New Roman, 五号, Not Expanded by / Condensed by

Formatted: Font: (Default) Times New Roman, 五号

Formatted: Font: (Default) Times New Roman, 五号, Not Expanded by / Condensed by

Formatted: Font: (Default) Times New Roman, 五号

Formatted: Font: (Default) Times New Roman, 五号, Not Expanded by / Condensed by

Formatted: Font: (Default) Times New Roman, 五号

Formatted: Font: (Default) Times New Roman, 五号, Not Expanded by / Condensed by

Formatted: Font: (Default) Times New Roman, 五号

Formatted: Font: (Default) Times New Roman, 五号, Not Expanded by / Condensed by

Formatted: Font: (Default) Times New Roman, 五号

Formatted: Font: (Default) Times New Roman, 五号, Not Expanded by / Condensed by

Formatted: Font: (Default) Times New Roman, 五号

Formatted: Font: (Default) Times New Roman, 五号, Not Expanded by / Condensed by

Formatted: Font: (Default) Times New Roman, 五号

Formatted: Font: (Default) Times New Roman, 五号, Not Expanded by / Condensed by

Formatted: Font: (Default) Times New Roman, 五号

Formatted: Font: (Default) Times New Roman, 五号, Not Expanded by / Condensed by

Formatted: Font: (Default) Times New Roman, 五号

Formatted: Font: (Default) Times New Roman, 五号, Not Expanded by / Condensed by

Formatted: Font: (Default) Times New Roman, 五号

Formatted: Font: (Default) Times New Roman, 五号, Not Expanded by / Condensed by variations in wave amplitude are governed by a nonlinear energy dissipation, where hydrodynamic forces follow a quadratic dependence on the velocity. In the case of light cliff collapses, the dynamic responses result in complex absorption and distribution, whereas heavier cliff collapses promote wave reflection along with nonlinear effects of wave breaking and splash-induced turbulence, as can be observed in Fig. 5 (b, e&h). Conversely, the wave runup exhibits a linear relation with cliff mass, and this is due to the law of conservation of momentum, such that the resisting inertial force is directly proportional to cliff mass. The greater resistance to motion of heavier cliffs allows more energy to be conserved and utilized for higher wave runups before dissipation. The main difference between the two trends is that the wave amplitude is controlled by localized energy losses, whereas runup is governed by bulk momentum transfer rather than localized losses.

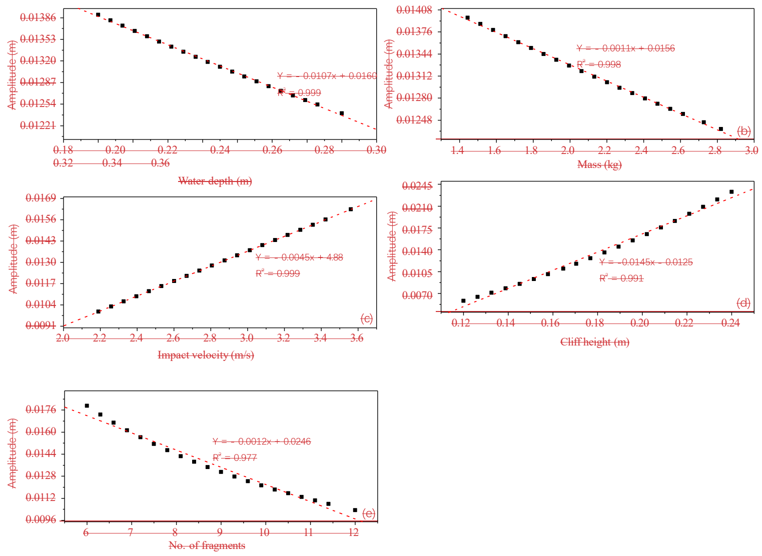

Formatted: Header

Formatted: Normal (Web), Justified, Indent: First line: 0.74 cm, Space Before: 0 pt, Line spacing: 1.5 lines, No bullets or numbering, Pattern: Clear (White), Tab stops: Not at 5.87 ch

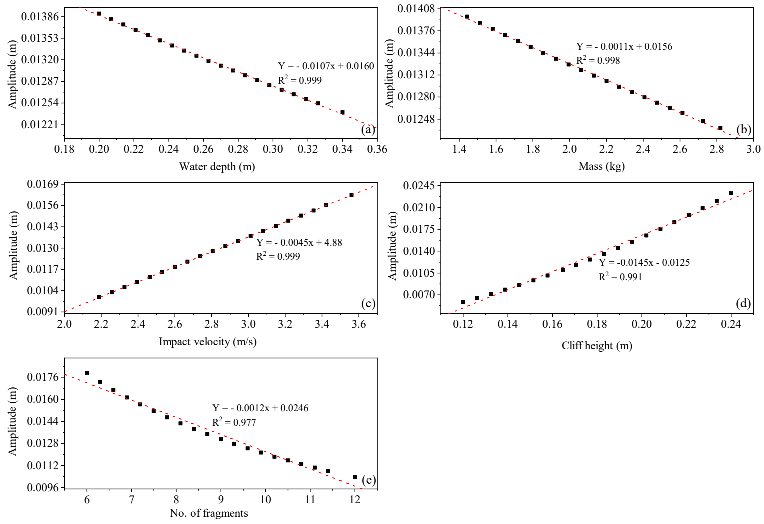

Fig. 18 Parametric analysis for wave amplitude (a) water depth, (b) cliff mass, (c) impact velocity, (d) cliff height, (e) number of fragments.

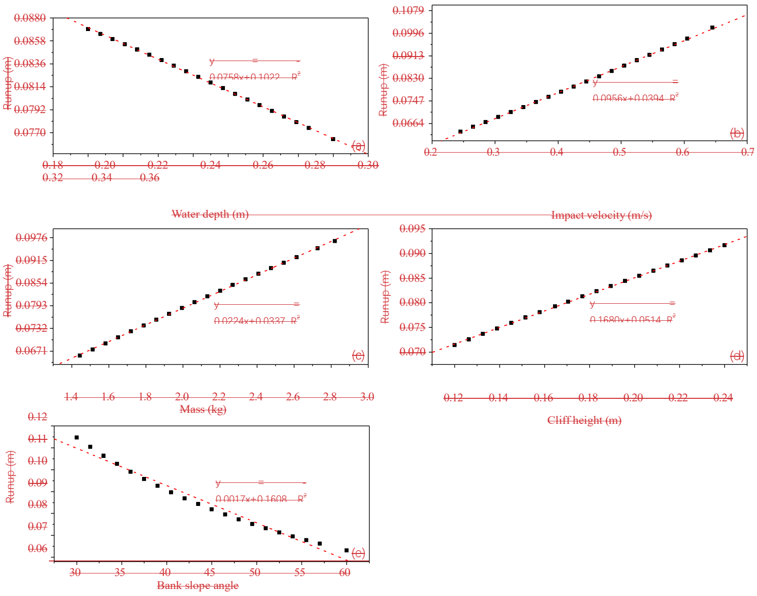

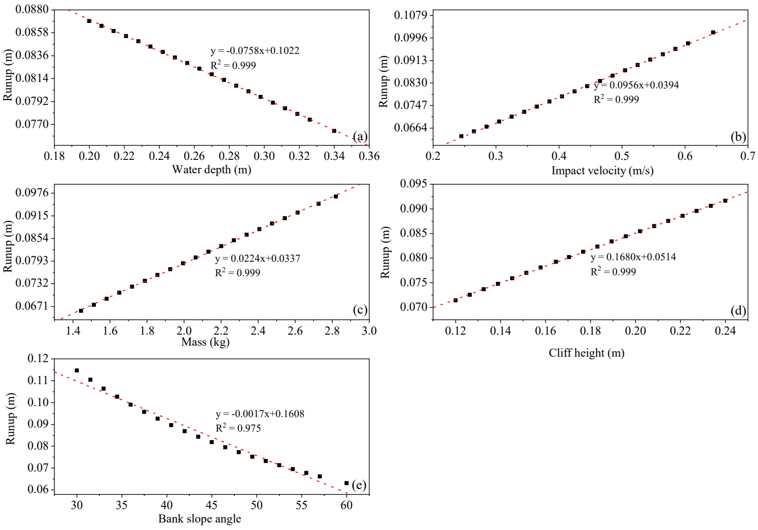

Fig. 19 Parametric analysis for wave runup (a) water depth, (b) impact velocity, (c) mass of the cliff, (d) cliff height, (e) bank slope angle.

4. Conclusions

While designing wave protection structures along the banks of reservoirs, it is

Formatted: Header

Formatted

Formatted

Formatted: Normal, Centered, Don't adjust right indent when grid is defined, Space After: 0.5 line, Line spacing: single, No bullets or numbering, Don't adjust space between Latin and Asian text, Don't adjust space between Asian text and numbers, Tab stops: Not at 13.31 ch

Formatted: Font: (Default) Times New Roman, 小四, Bold, Not Expanded by / Condensed by

Formatted: Font: (Default) Times New Roman, Pattern: Clear (White) common to use the empirical relations developed for granular flows, i.e., landslides and avalanches, to predict the amplitude and runup of the waves. However, the waves induced by various types of slides behave differently and should be treated accordingly. The dynamics of the waves induced by falling cliffs are entirely different from the waves induced by continuous granular flows. Similarly, the dynamics of the waves induced by falling cliffs following different types of motion (translational, rotational) are also different. This study aimed to develop a novel wave amplitude and runup prediction model for waves induced by rotational fall of the cliff using a combination of seven governing parameters, and then compare it with the dynamics of the wave induced by continuous granular flows. Based on the results and discussions, the study concludes as follows,

~~1.~~ It was concluded that water depth strongly controls the shape of the induced splash ~~depends on water depth;~~

~~increased depth forms a~~ and wave amplification. Shallow water induced elongated, tall splashes, and higher wave amplitudes; in contrast, deep water produced mushroom-shaped ~~splash, whereas shallow water forms a~~

Formatted: Header

Formatted: Font: (Default) Times New Roman, Pattern: Clear (White)

Formatted: Font: (Default) Times New Roman, Pattern: Clear (White)

Formatted: Font: (Default) Times New Roman, Pattern: Clear (White)

Formatted: Font: (Default) Times New Roman, Pattern: Clear (White)

Formatted: Font: (Default) Times New Roman, Pattern: Clear (White)

Formatted: Font: (Default) Times New Roman, Pattern: Clear (White)

Formatted: Font: (Default) Times New Roman, Pattern: Clear (White)

Formatted: Font: (Default) Times New Roman, Pattern: Clear (White)

Formatted: Font: (Default) Times New Roman, Pattern: Clear (White)

Formatted: Font: (Default) Times New Roman, Pattern: Clear (White)

Formatted: Font: (Default) Times New Roman, Pattern: Clear (White)

Formatted: Normal, Indent: First line: 0.63 cm, Line spacing: 1.5 lines, No bullets or numbering, Tab stops: Not at 5.87 ch

Formatted: Font: (Default) Times New Roman, Font color: Red, Pattern: Clear (White)

Formatted: Font: (Default) Times New Roman, Font color: Red, Pattern: Clear (White)

Formatted: Font: (Default) Times New Roman, Font color: Red, Pattern: Clear (White)

~~vertically elongated splash. Moreover, shallow water allows more amplification of~~

1. ~~waves for the same~~splashes with higher energy ~~level compared to deep water~~dissipation and lower wave amplitudes.

~~2.~~ The ~~effect of viscous forces is very, very small and can be ignored, since the Reynolds~~higher values of Froude number (> 1.2) for all the experiments ~~is very high, thus leaving~~indicate that the viscous effects were negligible, so the Froude

2. number was selected as the ~~best possible~~most suitable dynamic scaling factor~~. It is concluded that the Froude~~ for describing the behaviour of the waves.

~~number also increases as the water depth decreases.~~

3. ~~3.~~ The ~~study concludes that~~ wave amplitude ~~is~~was greatly influenced by cliff height~~,~~ (51 %), number of fragments (22 %), Impact velocity (18 %), cliff mass (4.69 %), and water depth (4.36 %). Whereas the wave runup was governed by the runup slope angle, impact velocity, and cliff mass.

~~impact velocity, and the number of fragments. For all the cases, the deep water dissipated more energy compared to shallow waters, thus resulting in lower amplitudes.~~

~~4.~~ The amplitude of the wave induced by equivalent granular mass ~~is~~sliding on a 30° slope was 28-42% lower than the waves induced by rotational cliff collapse, thus concluding that the mode of energy

4. transfer to the water body plays a critical role in wave dynamics.

~~5. A second level validation of the developed model was performed by conducting sensitivity and parametric analysis. It is concluded that the amplitude is highly sensitive to any change in cliff height, impact velocity, and number of fragments. In contrast, runup greatly depends on runup slope angle, impact velocity, and mass of the cliff.~~

5. A novel MEP-based prediction model was developed for wave amplitude and runup. The model showed great performance during the training and testing stage, and showed high sensitivity to the used parameters, thus confirming its reliability.
6. Research findings highlight that accurate hazard assessment of the cliff collapse requires models that account for the rotational failure mode and the fragmentation upon impact with the water surface. Traditional granular slide models may result in an underestimation of the initial wave amplitude and energy transferred.

Funding

This work was supported by the ~~National Key R&D Program of~~ China ~~(Grant No. 2023YFC3007001), the China~~ Postdoctoral Science Foundation (Grant ~~no.~~ No. 2024M762420), the National Natural Science Foundation of China (Grant ~~no.~~No. 42120104008), and the National Natural Science Foundation of China (Grant No. 42202312), and the Fundamental Research Funds for the Central Universities.

Author contributions

Formatted: Header

Formatted

Formatted: Space Before: 0 pt, After: 8 pt, Don't add space between paragraphs of the same style, Line spacing: 1.5 lines, Numbered + Level: 1 + Numbering Style: 1, 2, 3, … + Start at: 1 + Alignment: Left + Aligned at: 0 cm + Indent at: 0.78 cm, Tab stops: Not at 7.97 ch

Formatted: Font: (Default) Times New Roman, Font color: Red, Pattern: Clear (White)

Formatted

Formatted

Formatted: Space After: 8 pt, Don't add space between paragraphs of the same style, Line spacing: 1.5 lines, Numbered + Level: 1 + Numbering Style: 1, 2, 3, … + Start at: 1 + Alignment: Left + Aligned at: 0 cm + Indent at: 0.78 cm, Tab stops: Not at 7.97 ch

Formatted

Formatted: Space After: 8 pt, Don't add space between paragraphs of the same style, Line spacing: 1.5 lines, Numbered + Level: 1 + Numbering Style: 1, 2, 3, … + Start at: 1 + Alignment: Left + Aligned at: 0 cm + Indent at: 0.78 cm, Tab stops: Not at 5.87 ch + 7.97 ch

Formatted

Formatted: Font: (Default) Times New Roman, Font color: Red, Pattern: Clear (White)

Formatted: Font: (Default) Times New Roman, Font color: Red, Pattern: Clear (White)

Formatted: Space After: 8 pt, Don't add space between paragraphs of the same style, Line spacing: 1.5 lines, Numbered + Level: 1 + Numbering Style: 1, 2, 3, … + Start at: 1 + Alignment: Left + Aligned at: 0 cm + Indent at: 0.78 cm, Tab stops: Not at 7.97 ch

Formatted: Font: (Default) Times New Roman, 小四, Bold, Not Expanded by / Condensed by

Formatted: Normal, Don't adjust right indent when grid is defined, Space Before: 0 pt, After: 0.5 line, No bullets or numbering, Don't adjust space between Latin and Asian text, Don't adjust space between Asian text and numbers, Tab stops: Not at 5.87 ch

Formatted

Formatted

Formatted

Formatted: Normal, Indent: First line: 0.74 cm, Line spacing: 1.5 lines, No bullets or numbering, Tab stops: Not at 5.87 ch

Formatted

HG wrote the manuscript and performed the experiments, TK performed numerical modeling, XL designed the research, TMS helped in writing the manuscript, YH supervised the project, and ZC helped in conducting experiments.

Declarations

Competing interests: The authors declare no competing interests.

References

Alavi, A.H., Gandomi, A.H., Nejad, H.C., Mollahasani, A., Rashed, A., 2013. Design equations for prediction of pressuremeter soil deformation moduli utilizing

Formatted: Header

Formatted: Font: (Default) Times New Roman, (Asian) +Body Asian (等线), 小四, Bold, Not Expanded by / Condensed by , Ligatures: None

Formatted: Font: (Default) Times New Roman, (Asian) +Body Asian (等线)

Formatted: Normal, Don't adjust right indent when grid is defined, Space Before: 0 pt, After: 0.5 line, Line spacing: 1.5 lines, No bullets or numbering, Don't adjust space between Latin and Asian text, Don't adjust space between Asian text and numbers, Tab stops: Not at 5.87 ch

Formatted: Font: (Default) Times New Roman, (Asian) +Body Asian (等线), Ligatures: None

Formatted: Font: (Default) Times New Roman, (Asian) +Body Asian (等线), Not Expanded by / Condensed by , Ligatures: None

Formatted: Font: (Default) Times New Roman, (Asian) +Body Asian (等线), Ligatures: None

Formatted: Font: (Default) Times New Roman, (Asian) +Body Asian (等线), Not Expanded by / Condensed by , Ligatures: None

Formatted: Font: (Default) Times New Roman, (Asian) +Body Asian (等线), Ligatures: None

Formatted: Font: (Default) Times New Roman, (Asian) +Body Asian (等线), Not Expanded by / Condensed by , Ligatures: None

Formatted: Font: (Default) Times New Roman, (Asian) +Body Asian (等线), Ligatures: None

Formatted: Font: (Default) Times New Roman, (Asian) +Body Asian (等线), Not Expanded by / Condensed by , Ligatures: None

Formatted: Font: (Default) Times New Roman, (Asian) +Body Asian (等线), Ligatures: None

Formatted: Font: (Default) Times New Roman, (Asian) +Body Asian (等线), Not Expanded by / Condensed by , Ligatures: None

Formatted: Font: (Default) Times New Roman, (Asian) +Body Asian (等线), Ligatures: None

Formatted: Font: (Default) Times New Roman, (Asian) +Body Asian (等线), Not Expanded by / Condensed by , Ligatures: None

Formatted: Font: (Default) Times New Roman, (Asian) +Body Asian (等线), Ligatures: None

Formatted: Font: (Default) Times New Roman, (Asian) +Body Asian (等线), Not Expanded by / Condensed by , Ligatures: None

Formatted: Font: (Default) Times New Roman, (Asian) +Body Asian (等线), Ligatures: None

Formatted: Font: (Default) Times New Roman, 小四, Bold, Not Expanded by / Condensed by

Formatted: Normal, Space Before: 0 pt, No bullets or numbering, Tab stops: Not at 5.87 ch

expression programming systems. Neural Comput. Appl. 23, 1771–1786. https://doi.org/10.1007/s00521-012-1144-6

Alavi, A.H., Gandomi, A.H., Sahab, M.G., Gandomi, M., 2010. Multi expression programming: A new approach to formulation of soil classification. Eng. Comput. 26, 111–118. https://doi.org/10.1007/s00366-009-0140-7https://doi.org/10.1007/s00366-009-0140-7.

Aidun, C.K., Clausen, J.R., 2010. Lattice-boltzmann method for complex flows. Annu. Rev.Bellotti, G., Romano, A., 2017. Wavenumber-frequency analysis of landslide-generated tsunamis at a conical island. Part II: EOF and modal analysis. Coast. Eng. 128, 84–91. https://doi.org/10.1016/j.coastaleng.2017.07.008
Fluid Mech. 42, 439–472. https://doi.org/10.1146/annurev-fluid-121108-145519

Backbill, J.U., Kothe, D.B., Zemach, C., 1992. for Modeling Surface Tension *. J Comput Phys 100, 335–354.

Bougouin, A., Paris, R., Roche, O., 2020. Impact of Fluidized Granular Flows into Water Water: Implications for Tsunamis Generated by Pyroclastic Flows. J. Geophys. Res. Solid Earth 1–17. https://doi.org/10.1029/2019JB018954

Boultbee, N., Stead, D., Schwab, J., Geertsema, M., 2006. The Zymoetz River rock avalanche, June 2002, British Columbia, Canada. Eng Geol 83, 76–93. https://doi.org/10.1016/j.enggeo.2005.06.038 avalanche, June 2002, British Columbia, Canada. Eng. Geol. 83, 76–93. https://doi.org/10.1016/j.enggeo.2005.06.038

Brackbill, J.U., D.B. Kothe, and C. Zemach, *A continuum method for modeling surface tension.* Journal of computational physics, 1992. 100(2): p. 335-354.

Bujak, D., Ilic, S., Miliˇ, H., 2023. Wave Runup Prediction and Alongshore Variability on a Pocket Gravel Beach under Fetch-Limited Wave Conditions. J. Mar. Sci. Eng.

Cesario, E., Giampá, S., Baglione, E., Cordrie, L., Selva, J., Talia, D., 2024. Machine Learning for Tsunami Waves Forecasting Using Regression Trees. Big Data Res. Research 36, 100452. https://doi.org/10.1016/j.bdr.2024.100452

Dai, Z., Li, X., Lan, B., 2023. Three-Dimensional Modeling of Tsunami Waves Triggered by Submarine Landslides Based on the Smoothed Particle Hydrodynamics Method. J Mar Sci Eng 11. https://doi.org/10.3390/jmse11102015

Das, M.M., Wiegel, L.. R., 1972. Waves Generated by Horizontal Motion of a Wall. J. Waterw. Harb. Journal of the waterways, harbors and costal Eng. Div. engineering divison 98.

Dignan, J., Hayward, M.W., Salmanidou, D., Heidarzadeh, M., Guillas, S., 2023. Probabilistic Landslide Tsunami Estimation in the Makassar Strait, Indonesia, Using Statistical Emulation. Earth and Space Science 10. https://doi.org/10.1029/2023EA002951

Esposti Ongaro, T., de' Michieli Vitturi, M., Cerminara, M., Fornaciai, A., Nannipieri, L., Favalli, M., Calusi, B., Macías, J., Castro, M.J., Ortega, S., González-Vida, J.M., Escalante, C., 2021. Modeling Tsunamis Generated by Submarine Landslides at Stromboli Volcano (Aeolian Islands, Italy): A Numerical Benchmark Study. Front Earth Sci (Lausanne) 9. https://doi.org/10.3389/feart.2021.628652

Franci, A., Cremonesi, M., Perego, U., Crosta, G., Oñate, E., 2020. 3D simulation of Vajont disaster. Part 1: Numerical formulation and validation. Eng. Geol. 279., 105854. https://doi.org/10.1016/j.enggeo.2020.105854

Franco, A., Moernaut, J., Schneider-Muntau, B., Strasser, M., Gems, B., 2020. TheThe 1958 Lituya

Formatted: Header
Formatted
Formatted
Formatted
Formatted: Font: (Default) Times New Roman, Font color: Black
Formatted: Normal, Indent: Left: 0.85 cm, Hanging: 4.8 ch, Line spacing: single, No bullets or numbering, Don't adjust space between Latin and Asian text, Don't adjust space between Asian text and numbers, Tab stops: Not at 8.16 ch
Formatted: Font: (Default) Times New Roman, (Asian) +Body Asian (等线), Not Expanded by / Condensed by
Formatted: Font: (Default) Times New Roman, Font color: Black
Formatted
Formatted
Formatted
Formatted: Normal, Indent: Left: 0.85 cm, Hanging: 4.8 ch, Line spacing: single, No bullets or numbering, Don't adjust space between Latin and Asian text, Don't adjust space between Asian text and numbers, Tab stops: Not at 8.16 ch
Formatted
Formatted: Font: (Default) Times New Roman, Font color: Black
Formatted: Font: (Default) Times New Roman, Font color: Black
Formatted
Formatted
Formatted: Normal, Indent: Left: 0.85 cm, Hanging: 4.8 ch, Line spacing: single, No bullets or numbering, Don't adjust space between Latin and Asian text, Don't adjust space between Asian text and numbers, Tab stops: Not at 8.16 ch
Formatted
Formatted
Formatted
Formatted: Normal, Indent: Left: 0.85 cm, Hanging: 4.8 ch, Line spacing: single, No bullets or numbering, Don't adjust space between Latin and Asian text, Don't adjust space between Asian text and numbers, Tab stops: Not at 8.16 ch
Formatted: Font: (Default) Times New Roman, Font color: Black
Formatted
Formatted
Formatted: Normal, Indent: Left: 0.85 cm, Hanging: 4.8 ch, Line spacing: single, No bullets or numbering, Don't adjust space between Latin and Asian text, Don't adjust space between Asian text and numbers, Tab stops: Not at 8.16 ch
Formatted: Font: (Default) Times New Roman, Font color: Black
Formatted
Formatted
Formatted
Formatted
Formatted

Bay tsunami - Pre-event bathymetry reconstruction and 3D numerical modelling utilising the computational fluid dynamics software Flow-3D. Natural Hazards and Earth System Sciences 20, 2255–2279. https://doi.org/10.5194/nhess-20-2255-2020.

1958 Lituya Bay tsunami – Pre-event bathymetry reconstruction and 3D numerical modelling utilising the computational fluid dynamics software Flow-3D. Nat. Hazards Earth Syst. Sci. 20, 2255–2279. https://doi.org/10.5194/nhess-20-2255-2020

Fritz, H., Hager, W., Minor, H., 2004. Near field characteristics of landslide generated impulse waves. J Waterw. Waterway Port Coast. Coastal and Ocean Eng. 130, 287–302.

Formatted: Header

Formatted: Font: (Default) Times New Roman, Font color: Black

Formatted: Font: (Default) Times New Roman, Font color: Black

Formatted: Font: (Default) Times New Roman, Font color: Black, Not Expanded by / Condensed by

Formatted: Font: (Default) Times New Roman, Font color: Black

Formatted: Font: (Default) Times New Roman, Font color: Black, Not Expanded by / Condensed by

Formatted: Font: (Default) Times New Roman, Font color: Black

Formatted: Font: (Default) Times New Roman, Font color: Black, Not Expanded by / Condensed by

Formatted: Font: (Default) Times New Roman, Font color: Black

Formatted: Font: (Default) Times New Roman, Font color: Black, Not Expanded by / Condensed by

Formatted: Font: (Default) Times New Roman, Font color: Black

Formatted: Font: (Default) Times New Roman, Font color: Black, Not Expanded by / Condensed by

Formatted: Font: (Default) Times New Roman, Font color: Black

Formatted: Font: (Default) Times New Roman, Font color: Black, Not Expanded by / Condensed by

Formatted: Font: (Default) Times New Roman, Font color: Black

Formatted: Font: (Default) Times New Roman, Font color: Black, Not Expanded by / Condensed by

Formatted: Font: (Default) Times New Roman, Font color: Black

Formatted: Font: (Default) Times New Roman, Font color: Black, Not Expanded by / Condensed by

Formatted: Font: (Default) Times New Roman, Font color: Black, Not Expanded by / Condensed by

Formatted: Font: (Default) Times New Roman, Font color: Black

Formatted: Font: (Default) Times New Roman, Font color: Black, Not Expanded by / Condensed by

Formatted: Font: (Default) Times New Roman, Font color: Black, Not Expanded by / Condensed by

Formatted: Font: (Default) Times New Roman, Font color: Black

Formatted: Font: (Default) Times New Roman, Font color: Black, Not Expanded by / Condensed by

Formatted: Font: (Default) Times New Roman, Font color: Black

Formatted: Font: (Default) Times New Roman, Font color: Black, Not Expanded by / Condensed by

Formatted: Font: (Default) Times New Roman, Font color: Black

Formatted: Font: (Default) Times New Roman, Font color: Black, Not Expanded by / Condensed by

Formatted: Font: (Default) Times New Roman, Font color: Black

Formatted ...

Fritz, H.M., Hager, W.H., Minor, H.E., 2003. Landslide generated impulse waves. 1. Instantaneous flow fields. Exp~~.~~ Fluids 35, 505–519. https://doi.org/10.1007/s00348-003-0659-0

Gardezi, H., ~~Bilal, M., Cheng, Q., Xing, A., Zhuang, Y., Masood, T., 2021. A comparative analysis of attabad landslide on january 4, 2010, using two numerical models. Nat. Hazards 107, 519–538. https://doi.org/10.1007/s11069-021-04593-0~~

~~Gardezi, H.,~~ Ikrama, M., Usama, M., Iqbal, M., Jalal, F.E., Hussain, A., Li, X., 2024. Predictive modeling of rutting depth in modified asphalt mixes using gene-expression programming (GEP): A sustainable use of RAP, fly ash, and plastic waste. Constr~~.~~ Build~~.~~ Mater~~.~~ 443, 137809. https://doi.org/10.1016/j.conbuildmat.2024.137809

Grilli, S.T., ~~Shelby, M., Kimmoun, O., Dupont, G., Nicolsky~~Tappin, D.~~, Ma, G.,~~ R., Carey, S., Watt, S.F.L., Ward, S.N., Grilli, A.R., Engwell, S.L., Zhang, C., Kirby, J.T., ~~Shi, F., 2017. Modeling coastal~~ Schambach, L., Muin, M., 2019. Modelling of the tsunami ~~hazard~~ from ~~submarine mass failures: effect of slide rheology, experimental validation, and case studies off the US East Coast. Nat. Hazards 86, 353–391.~~the December 22, 2018 lateral collapse of Anak Krakatau volcano in the Sunda Straits, Indonesia. Sci Rep 9, 1–13. https://doi.org/10.~~1007/s11069-016-2692-3~~1038/s41598-019-48327-6

Guan, X., Shi, H., 2023. Translational momentum of deformable submarine landslides off a slope. J Fluid Mech 960, 1–41. https://doi.org/10.1017/jfm.2023.177

Gylfadóttir, S.S., Kim, J., Helgason, J.K., Brynjólfsson, S., Höskuldsson, Á., Jóhannesson, T., Harbitz, C.B., Løvholt, F., 2017. The 2014 Lake Askja rockslide-induced tsunami: Optimization of numerical tsunami model using observed data. J~~.~~ Geophys~~.~~ Res~~. Ocean.~~ Oceans 122, 4110–4122. https://doi.org/10.1002/2016JC012496

Heidarzadeh, M., Ishibe, T., Sandanbata, O., Muhari, A., Wijanarto, A.B., 2020. Numerical modeling of the subaerial landslide source of the 22 December 2018 Anak Krakatoa volcanic tsunami, Indonesia. Ocean Engineering 195, 106733. https://doi.org/10.1016/j.oceaneng.2019.106733

Heller, V., 2007. Landslide Generated Impulse Waves: Prediction of Near Field Characteristics (Doctoral dissertation, Eth Zurich).

Heller, V., ~~Ruffini~~Attili, T., Chen, F., Gabl, R., Wolters, G., ~~2023. A critical review about generic subaerial~~2021. Large-scale investigation into iceberg-tsunamis generated by various iceberg calving mechanisms.

Heller, V., Spinneken, J., 2015. On the effect of the water body geometry on landslide-tsunamis: Physical insight from laboratory tests and 2D to 3D wave parameter transformation. Coastal Engineering 104, 113–134. https://doi.org/10.1016/j.coastaleng.2015.06.006

Heller, V., Spinneken, J., 2013. Improved landslide-tsunami ~~experiments~~prediction: Effects of block model parameters and ~~options for a needed step change. Earth-Science~~ slide model. J Geophys Res Oceans 118, 1489–1507.~~Rev. 242, 104459.~~ https://doi.org/10.~~1016/j.earscirev.2023.104459~~1002/jgrc.20099

Higman, B., Shugar, D.H., Stark, C.P., Ekström, G., Koppes, M.N., Lynett, P., Dufresne, A., Haeussler, P.J., Geertsema, M., Gulick, S., Mattox, A., Venditti, J.G.,

Formatted: Header

Formatted: Font: (Default) Times New Roman, Font color: Black

Formatted: Normal, Indent: Left: 0.85 cm, Hanging: 4.8 ch, Line spacing: single, No bullets or numbering, Don't adjust space between Latin and Asian text, Don't adjust space between Asian text and numbers, Tab stops: Not at 8.16 ch

Formatted: Font: (Default) Times New Roman, Font color: Black

Walton, M.A.L., McCall, N., Mckittrick, E., MacInnes, B., Bilderback, E.L., Tang, H., Willis, M.J., Richmond, B., Reece, R.S., Larsen, C., Olson, B., Capra, J., Ayca, A., Bloom, C., Williams, H., Bonno, D., Weiss, R., Keen, A., Skanavis, V., Loso, M., 2018. The 2015 landslide and tsunami in Taan Fiord, Alaska. Sci. Rep. 8, 1–12. https://doi.org/10.1038/s41598-018-30475-w

Hirt, C.W. and B.D., Nichols, B.D., 1981. Volume of *fluid* (Fluid (VOF) *method*) Method for the *dynamics*Dynamics of *free boundaries*. Journal of computational physics, 1981. **39**(1): p.Free Boundaries *. J Comput Phys 225, 201––225.

Huang, B., Yin, Y., Liu, G., Wang, S., Chen, X., Huo, Z., 2012. Analysis of waves generated by Gongjiafang landslide in Wu Gorge, three Gorges reservoir, on

Formatted: Header

Formatted

Formatted

Formatted

Formatted

Formatted: Font: (Default) Times New Roman, Font color: Black

Formatted

Formatted: Normal, Indent: Left: 0.85 cm, Hanging: 4.8 ch, Line spacing: single, No bullets or numbering, Don't adjust space between Latin and Asian text, Don't adjust space between Asian text and numbers, Tab stops: Not at 8.16 ch

Formatted

Formatted

Formatted

Formatted: Normal, Indent: Left: 0.85 cm, Hanging: 4.8 ch, Line spacing: single, No bullets or numbering, Don't adjust space between Latin and Asian text, Don't adjust space between Asian text and numbers, Tab stops: Not at 9.3 ch

Formatted

November 23, 2008. Landslides 9, 395–405. https://doi.org/10.1007/s10346-012-0331-y

Huber, A., Hager, W., 1997. Forecasting impulse waves in reservoirs, in: Proc 19th Congrès Des Grands Barrages, Florence, ICOLD, Paris. pp. 993–1005.

Kamphuis, J., Bowering, R., 1970. Kamphuis JW, Bowering RJ (1970) Impulse waves generated by landslides, in: Proc 12th Coastal Eng 1:575–588, ASCE, Washing Ton, USA.

generated by landslides, in: Proc 12th Coastal Eng 1:575–588, ASCE, Washing Ton, USA.

Khan, K., Ashfaq, M., Iqbal, M., Khan, M.A., Amin, M.N., Shalabi, F.I., Faraz, M.I., Jalal, F.E., 2022. Multi Expression Programming Model for Strength Prediction of Fly-Ash-Treated Alkali-Contaminated Soils. Materials (Basel). 15. https://doi.org/10.3390/ma15114025

Kim, G.B., Cheng, W., Sunny, R.C., Horrillo, J.J., McFall, B.C., Mohammed, F., Fritz, H.M., Beget, J., Kowalik, Z., 2020. Three Dimensional Landslide Generated Tsunamis: Numerical and Physical Model Comparisons. Landslides 17, 1145–1161. https://doi.org/10.1007/s10346-019-01308-2

Kubota, Y., Mochizuki, O., 2009. Splash Formation by a Spherical Body Plunging into Water. J. Vis. (Tokyo) 12, 339–346.

Li, Y., Ding, Y., Yang, L., Liu, X., Liu, Y., 2023a. A prediction model for the rockslide-generated wave amplitude under the condition of bedrock mass breakup. Ocean Eng. Engineering 272, 113845. https://doi.org/10.1016/j.oceaneng.2023.113845

Li, Y., Ding, Y.N., Yang, L., Liu, X.S., Liu, Y., 2023b. A prediction model for the rockslide-generated wave amplitude under the condition of bedrock mass breakup. Ocean Eng. Engineering 272. https://doi.org/10.1016/j.oceaneng.2023.113845

Li, Y., Peng, T., Xiao, L., Wei, H., Li, X., 2024. Wave runup prediction for a semi-submersible based on temporal convolutional neural network. Journal of Ocean Engineering and Science 9, 528–540. https://doi.org/10.1016/j.joes.2022.08.005

submersible based on temporal convolutional neural network. J. Ocean Eng. Sci. 9, 528–540. Lindstrøm, E.K., 2016. Waves generated by subaerial slides with various porosities. Coastal Engineering 116, 170–179. https://doi.org/10.1016/j.joes.2022.08.005coastaleng.2016.07.001

Lindstrøm, E.K., Pedersen, G.K., Jensen, A., Glimsdal, S., 2014. Experiments on slide generated waves in a 1:500 scale fjord model. Coastal Engineering 92, 12–23. https://doi.org/10.1016/j.coastaleng.2014.06.010

Lipiejko, N., Whittaker, C.N., Lane, E.M., Power, W.L., 2023. Wave Generation by Fluidized Granular Flows Flows: Experimental Insights Into the Maximum Near-Field Wave Amplitude. J. Geophys. Res. Ocean. Oceans. https://doi.org/10.1029/2022JC019583.

Liu, M. and G. Liu, *Smoothed particle hydrodynamics (SPH): an overview and recent developments.* Liu, J., Heller, V., Wang, Y., Yin, K., 2025. Investigation of subaerial landslide–tsunamis generated by different mass movement types using smoothed particle hydrodynamics. Eng Geol 352. https://doi.org/10.1016/j.enggeo.2025.108055

Liu, M.B., Liu, G.R., 2010. Smoothed Particle Hydrodynamics (SPH): an Overview and Recent Developments. Archives of computational methods in engineering, 2010. 17: p. 25 17, 25–76. https://doi.org/10.1007/s11831-010-9040-7

76.

Maciel, G.D.F., Pereira, J.B., Sáo, Y.T., Ferreira, F.D.O., Ferreira, L.G., n.d. Impulse wave in the Brazilian Lake of Capitólio.

McFall, B.C., Fritz, H.M., 2016. Physical modelling of tsunamis generated by three-dimensional deformable granular landslides on planar and conical island slopes. Proceedings of the Royal Society A: Mathematical, Physical and Engineering Sciences 472. https://doi.org/10.1098/rspa.2016.0052

Miller, D.J., 19601960a. Giant waves in Lituya Bay, Alaska. Geol. Surv. Prof. Pap.Geological Survey Professional Paper No. 354

C C ; US Governement Print. Off.Printing Office: Washington, DC, USA 51–86.

Miller, D.J., 1960b. Giant waves in Lituya Bay, Alaska. Geological Survey Professional Paper No. 354 C ; US Governement Printing Office: Washington, DC, USA 51–86.

Mohammed, F., Fritz, H.M., 2012a. Physical modeling of tsunamis generated by three-dimensional deformable granular landslides. J Geophys Res Oceans 117, 1–20. https://doi.org/10.1029/2011JC007850

Mohammed, F., Fritz, H.M., 2012b. Physical modeling of tsunamis generated by three-dimensional deformable granular landslides. J. Geophys. Res. Ocean. Oceans 117, 1–20.

https://doi.org/10.1029/2011JC007850

Formatted: Header

Formatted: Font: (Default) Times New Roman, Font color: Black

Formatted

Formatted

Formatted

Formatted: Normal, Indent: Left: 0.85 cm, Hanging: 4.8 ch, Line spacing: single, No bullets or numbering, Don't adjust space between Latin and Asian text, Don't adjust space between Asian text and numbers, Tab stops: Not at 8.16 ch

Formatted

Formatted

Formatted: Font: (Default) Times New Roman, Font color: Black

Formatted

Formatted

Formatted

Formatted: Normal, Indent: Left: 0.85 cm, Hanging: 4.8 ch, Line spacing: single, No bullets or numbering, Don't adjust space between Latin and Asian text, Don't adjust space between Asian text and numbers, Tab stops: Not at 8.16 ch

~~Mohammed, F., Fritz, H.M., 2012b.~~ Mohammed, F., Fritz, H.M., 2012c. Physical modeling of tsunamis generated by three-dimensional deformable granular landslides. J~~.~~ Geophys~~.~~ Res~~.~~ 117. https://doi.org/10.1029/2011JC007850

Monaghan, J.J., 1994. Simulating free surface flows with SPH. ~~Journal of computational physics, 1994.~~ J Comput Phys 110~~(2): p.~~ 399–406.

Montagna, F., Bellotti, G., Di Risio, M., 2011. 3D numerical modeling of landslide-generated tsunamis around a conical island. Natural Hazards 58, 591–608. https://doi.org/10.1007/s11069-010-9689-0

Mulligan, R.P., Franci, A., Celigueta, M.A., Take, W.A., 2020. Simulations of Landslide Wave Generation and Propagation Using the Particle Finite Element Method. J Geophys Res Oceans 125, 1–17. https://doi.org/10.1029/2019JC015873

Myrhaug, D., Lader, P.F., 2019. Random wave-induced current in shallow water using deep water wind and wave statistics. ~~Marit. Eng.~~ Maritime Engineering 174, 1–20.

Noda, E., 1970. Water waves generated by landslides. J Water Port ~~Coast.~~ Coastal Ocean Div, Am Soc Civ Eng. 96, 835–855.

Panizzo, A., De Girolamo, P., Petaccia, A., 2005. Forecasting impulse waves generated by subaerial landslides. J Geophys Res Oceans 110, 1–23. https://doi.org/10.1029/2004JC002778 ~~by subaerial landslides. J. Geophys. Res. Ocean. 110, 1-23.~~

Paris, A., Heinrich, P., Abadie, S., 2021. Landslide tsunamis: Comparison between depth-averaged and Navier–Stokes models. Coastal Engineering 170, 104022. https://doi.org/10.1016/j.coastaleng.2021.104022

Rauter, M., Viroulet, S., Gylfadóttir, S.S., Fellin, W., Løvholt, F., 2022. Granular porous landslide tsunami modelling – the 2014 Lake Askja flank collapse. Nat Commun 13. https://doi.org/10.1038/s41467-022-28296-7

~~https://doi.org/10.1029/2004JC002778~~

Ró, G., Cerkowniak, G., 2024. Soft postglacial cliffs in Poland under climate change. oceanologia 66. https://doi.org/10.1016/j.oceano.2024.01.003

Romano, A., Lara, J.L., Barajas, G., Di Paolo, B., Bellotti, G., Di Risio, M., Losada, I.J., De Girolamo, P., 2020. Tsunamis Generated by Submerged Landslides: Numerical Analysis of the Near-Field Wave Characteristics. J Geophys Res Oceans 125, 1–26. https://doi.org/10.1029/2020JC016157

Romano, A., Lara, J.L., Barajas, G., Losada, Í.J., 2023. Numerical modeling of tsunamis generated by granular landslides in OpenFOAM®: A Coulomb viscoplastic rheology. Coastal Engineering 186, 104391. https://doi.org/10.1016/j.coastaleng.2023.104391

Romano, M., Romano, M., Liong, S., Vu, M.T., Zemskyy, P., Doan, C.D., Dao, M.H., Tkalich, P., 2009. Artificial neural network for tsunami forecasting. J~~.~~ Asian Earth Sci~~.~~ 36, 29–37. https://doi.org/10.1016/j.jseaes.2008.11.003

~~Sohag, M., et al.,~~ Ruffini, G., Heller, V., Briganti, R., 2019. Numerical ~~*study of drop spread and rebound on heated surfaces with consideration*~~ modelling of landslide-tsunami propagation in a wide range of ~~*high pressure.* Physics of Fluids, 2022. 34(11).~~

~~Sohag, M., W. Zhang, and X. Yang, *Three-dimensional numerical study of two drops impacting on a heated solid surface by smoothed particle hydrodynamics.* Physics of Fluids, 2023. **35**(12).~~

~~Takabatake, T., Han, D.C., Valdez, J.J., Inagaki, N., Mäll, M., Esteban, M., Shibayama,~~

Formatted: Header
Formatted: Font: (Default) Times New Roman, Font color: Black
Formatted
Formatted
Formatted: Font: (Default) Times New Roman, Font color: Black, Not Expanded by / Condensed by
Formatted
Formatted
Formatted: Normal, Indent: Left: 0.85 cm, Hanging: 4.8 ch, Line spacing: single, No bullets or numbering, Don't adjust space between Latin and Asian text, Don't adjust space between Asian text and numbers, Tab stops: Not at 8.16 ch
Formatted
Formatted
Formatted: Normal, Indent: Left: 0.85 cm, Hanging: 4.8 ch, Line spacing: single, Don't adjust space between Latin and Asian text, Don't adjust space between Asian text and numbers, Tab stops: Not at 9.3 ch
Formatted: Font color: Black
Formatted
Formatted
Formatted: Normal, Indent: Left: 0.85 cm, Hanging: 4.8 ch, Line spacing: single, Don't adjust space between Latin and Asian text, Don't adjust space between Asian text and numbers, Tab stops: Not at 8.16 ch
Formatted
Formatted
Formatted: Normal, Indent: Left: 0.85 cm, Hanging: 4.8 ch, Line spacing: single, Don't adjust space between Latin and Asian text, Don't adjust space between Asian text and numbers, Tab stops: Not at 8.16 ch
Formatted
Formatted
Formatted: Font: (Default) Times New Roman, Font color: Black, Not Expanded by / Condensed by
Formatted: Font: (Default) Times New Roman, Font color: Black
Formatted
Formatted
Formatted: Normal, Indent: Left: 0.85 cm, Hanging: 4.8 ch, Line spacing: single, No bullets or numbering, Don't adjust space between Latin and Asian text, Don't adjust space between Asian text and numbers, Tab stops: Not at 8.16 ch
Formatted: Font: (Default) Times New Roman, Font color: Black
Formatted
Formatted
Formatted
Formatted: Normal, Indent: Left: 0.85 cm, Hanging: 4.8 ch, Line spacing: single, No bullets or numbering, Don't adjust space between Latin and Asian text, Don't adjust space between Asian text and numbers, Tab stops: Not at 8.16 ch
Formatted
Formatted

~~T., 2022. Three Dimensional Physical Modeling of Tsunamis Generated by Partially Submerged Landslides. J. Geophys. Res. Ocean. 127.~~ idealised water body geometries. Coastal Engineering 153, 103518. https://doi.org/10.~~1029/2021JC017826~~1016/j.coastaleng.2019.103518

Sælevik, G., Jensen, A., Pedersen, G., 2009. Experimental investigation of impact generated tsunami; related to a potential rock slide, Western Norway. Coastal Engineering 56, 897–906. https://doi.org/10.1016/j.coastaleng.2009.04.007

Sun, S.W., Wen, Q., do Carmo Reis Cavalcanti, M., Yang, X.R., Wang, J.Q., 2024. Numerical and laboratory experiments on the toppling behavior of a massive single block: a case study of the Furnas Reservoir, Brazil. Landslides 21, 2327–2347. https://doi.org/10.1007/s10346-024-02288-8

Svennevig, K., Hicks, S.P., Forbriger, T., Lecocq, T., Widmer-Schnidrig, R., Mangeney, A., Hibert, C., Korsgaard, N.J., Lucas, A., Satriano, C., Anthony, R.E., Mordret, A., Schippkus, S., Rysgaard, S., Boone, W., Gibbons, S.J., Cook, K.L., Glimsdal, S., Løvholt, F., Van Noten, K., Assink, J.D., Marboeuf, A., Lomax, A., Vanneste, K., Taira, T., Spagnolo, M., De Plaen, R., Koelemeijer, P., Ebeling, C., Cannata, A., Harcourt, W.D., Cornwell, D.G., Caudron, C., Poli, P., Bernard, P., Larose, E., Stutzmann, E., Voss, P.H., Lund, B., Cannavo, F., Castro-Díaz, M.J., Chaves, E., Dahl-Jensen, T., De Pinho Dias, N., Déprez, A., Develter, R., Dreger, D., Evers, L.G., Fernández-Nieto, E.D., Ferreira, A.M.G., Funning, G., Gabriel, A.A., Hendrickx, M., Kafka, A.L., Keiding, M., Kerby, J., Khan, S.A., Dideriksen, A.K., Lamb, O.D., Larsen, T.B., Lipovsky, B., Magdalena, I., Malet, J.P., Myrup, M., Rivera, L., Ruiz-Castillo, E., Wetter, S., Wirtz, B., 2024. A rockslide-generated tsunami in a Greenland fjord rang Earth for 9 days. Science (1979) 385, 1196–1205. https://doi.org/10.1126/science.adm9247

Tarwidi, D., Redjeki, S., Adytia, D., Apri, M., 2023. MethodsX An optimized XGBoost-based machine learning method for predicting wave run-up on a sloping beach. MethodsX 10, 102119. https://doi.org/10.1016/j.mex.2023.102119

Tian, L., Lei, J., Mao, P., Xie, W., 2025. Landslide-Induced Wave Run-Up Prediction Based on Large-Scale Geotechnical Experiment : A Case Study of Wangjiashan Landslide Area of Baihetan Reservoir , China. Water (Basel). ~~Based on Large-Scale Geotechnical Experiment : A Case Study of Wangjiashan Landslide Area of Baihetan Reservoir , China. Water.~~

Tryggvason, G., Bunner, B., Esmaeeli, A., Juric, D., Al-Rawahi, N., Tauber, W., Han, J., Nas, S., Jan, Y.J., 2001. A Front-Tracking Method for the Computations of Multiphase Flow. J. Comput. Phys. 169, 708–759. https://doi.org/10.1006/jcph.2001.6726

Usama, ~~M~~Mr.M., Gardezi, H., Jalal, ~~M~~Mr.F.E., Rehman, ~~M~~Mr.M.A., Javed, ~~M~~Ms.N., Janjua, ~~D~~Dr.S., Iqbal, ~~M~~Mr.M., 2023. Predictive Modelling of Compression Strength of Waste Gp/Fa Blended Expansive Soils Using Multi-Expression Programming. Constr~~.~~ Build~~.~~

Formatted: Header

Formatted: Normal, Indent: Left: 0.85 cm, Hanging: 4.8 ch, Line spacing: single, No bullets or numbering, Don't adjust space between Latin and Asian text, Don't adjust space between Asian text and numbers, Tab stops: Not at 8.16 ch

Formatted: Font: (Default) Times New Roman, Font color: Black, Not Expanded by / Condensed by

Formatted: Font: (Default) Times New Roman, Font color: Black

Formatted: Font: (Default) Times New Roman, Font color: Black

Formatted

Formatted

Formatted

Formatted: Normal, Indent: Left: 0.85 cm, Hanging: 4.8 ch, Line spacing: single, No bullets or numbering, Don't adjust space between Latin and Asian text, Don't adjust space between Asian text and numbers, Tab stops: Not at 8.16 ch

Formatted

Formatted: Font: (Default) Times New Roman, Font color: Black

Formatted: Font: (Default) Times New Roman, Font color: Black

Formatted

Formatted

Formatted

Mater. 392, 131956. https://doi.org/10.2139/ssrn.4227552

Wang, J., Wang, S., Su, A., Xiang, W., Xiong, C., Blum, P., 2021. Simulating landslide-induced tsunamis in the Yangtze River at the Three Gorges in China. Acta Geotech. 16, 2487–2503. https://doi.org/10.1007/s11440-020-01131-3

Wang, J., Ward, S.N., Xiao, L., 2015. Numerical simulation of the december 4, 2007 landslide-generated tsunami in Chehalis Lake, Canada. Geophys. J. Int. 201, 372–376. https://doi.org/10.1093/gji/ggv026

Wang, W., Chen, G., Yin, K., Wang, Y., Zhou, S., Liu, Y., 2016. Modeling of landslide2016a. Modeling of landslide generated impulsive waves considering complex topography in reservoir area. Environ Earth Sci 75, 1–15. https://doi.org/10.1007/s12665-016-5252-y

Wang, W., Chen, G., Yin, K., Wang, Y., Zhou, S., Liu, Y., 2016b. Modeling of landslide generated impulsive waves considering complex topography in reservoir area. Environ. Earth Sci. 75, 1–15. https://doi.org/10.1007/s12665-016-5252-y

Wang, Y., Liu, J., Li, D., Yan, S., 2017a2017. Optimization model for maximum tsunami amplitude generated by riverfront landslides based on laboratory investigations. Ocean Eng. 142, 433–440. https://doi.org/10.1016/j.oceaneng.2017.07.030

Wang, Y., Liu, J., Li, D., Yan, S., 2017b. Optimization model for maximum tsunami amplitude generated by riverfront landslides based on laboratory investigations. Ocean Eng.Engineering 142, 433–440. https://doi.org/10.1016/j.oceaneng.2017.07.030

Ward, N. Steve, Day, Simon, 2011. The 1963 Landslide and Flood at Vaiont Reservoir Italy. A tsunami ball simulation. Ital. J. Geosci. 130, 16–26. https://doi.org/10.3301/ijg.2010.21

Watts, P., 1998a. Wavemaker Curves for Tsunamis Generated by Underwater Landslides. J. Waterw. Port, Coastal, Ocean Eng. 124, 127–137. https://doi.org/10.1061/(asce)0733-950x(1998)124:3(127)

Watts, P., 1998b.. Wavemaker curves for tsunamis generated by underwater landslides. J. Waterw. Port, Coast. Ocean Eng. 124, 1998.

Wiguna, E.A., 2022. Development of Real-Time Tsunami Early Warning System Dashboard Based on Tunami-F1 and Machine Learning in Sunda Arc, Indonesia, in: 2022 IEEE Ocean Engineering Technology and Innovation Conference: Management and Conservation for Sustainable and Resilient Marine and Coastal Resources (OETIC). IEEE, pp. 23–29. https://doi.org/10.1109/OETIC57156.2022.10176243

Wu, Y., Liu, L.-F.P., Hwang, K., Hwung, H.-H., 2018. A unified runup formula for breaking solitary waves on a uniform beach, in: Costal Engineering Proceedings.

Wunnemann, K., Weiss, R., 2015. The meteorite impact-induced tsunami hazard. Philosophical Transactions. Philos. Trans.

Yang, X., Kong, S., 2018. 3D Simulation of Drop Impact on Dry Surface. Int J Comput Methods 15, 1–23. https://doi.org/10.1142/S0219876218500111

910 Yarkoni, T., Westfall, J., 2019. Choosing prediction over explanation in psychology:
911 lessons from machine learning. Prospect psychol Sci. science 12, 1100–1122.
912 https://doi.org/10.1177/1745691617693393.Choosing

913 Yin, Y., Huang, B., Liu, G., Wang, S., Yang, X. and S. C. Kong, *3D Simulation of Drop Impact on Dry Surface Using SPH*
914 *Method*. International Journal of Computational Methods, 2018. 15(03): p.
915 1850011.
2015. Potential risk analysis on a Jianchuandong dangerous rockmass-generated impulse wave in the Three Gorges Reservoir, China. Environ Earth Sci 74, 2595–2607. https://doi.org/10.1007/s12665-015-4278-x

916 Young, A.P., Guza, R.T., Matsumoto, H., Merri, M.A., Reilly, W.C.O., Swirad, Z.M.,
917 2021. Geomorphology Three years of weekly observations of coastal cliff erosion
918 by waves and rainfall Mean Profile Change (m). Geomorphology 375.
919 https://doi.org/10.1016/j.geomorph.2020.107545

920

921 Zhao, T., Utili, S., Crosta, G.B., 2016. Rockslide and Impulse Wave Modelling in the
922 Vajont Reservoir by DEM-CFD Analyses. Rock Mech. Rock Eng. 49, 2437–2456.
923 https://doi.org/10.1007/s00603-015-0731-0
923

Formatted: Header
Formatted: Font: (Default) Times New Roman, Font color: Black
Formatted
Formatted
Formatted
Formatted
Formatted: Normal, Indent: Left: 0.85 cm, Hanging: 4.8 ch, Line spacing: single, No bullets or numbering, Don't adjust space between Latin and Asian text, Don't adjust space between Asian text and numbers, Tab stops: Not at 8.16 ch
Formatted
Formatted: Font: (Default) Times New Roman, Font color: Black
Formatted
Formatted: Font: (Default) Times New Roman, Font color: Black, Not Expanded by / Condensed by
Formatted
Formatted
Formatted
Formatted
Formatted: Normal, Indent: Left: 0.85 cm, Hanging: 4.8 ch, Line spacing: single, No bullets or numbering, Don't adjust space between Latin and Asian text, Don't adjust space between Asian text and numbers, Tab stops: Not at 8.16 ch
Formatted: Font: (Default) Times New Roman, 小四
Formatted: Indent: Left: 0 cm, Space Before: 0 pt
Formatted: Font: 小五
Formatted: Footer, Right: 0.63 cm, Line spacing: single